Welding in the World (2024) 68:1707–1730
https://doi.org/10.1007/s40194-024-01793-7

RESEARCH PAPER

Numerical simulation of multi-field coupling behavior and heat and mass transfer mechanism in laser additive manufacturing process

Xing Han[1] · Chang Li[1] · Han Sun[1] · Yichang Sun[1]

Received: 18 August 2023 / Accepted: 23 May 2024 / Published online: 30 May 2024

Abstract

The serviceability of cladding layers manufactured by laser depends on the microstructure formed by the metallurgical solidification. The microstructure in the clad layer is influenced by several factors. Among them, the elemental distribution state of the molten powder in the molten pool plays a dominant role. The diffusion distribution of elements is closely related to the non-equilibrium metallurgical behavior in the additive manufacturing process. Therefore, it is important to conduct an in-depth study on the multi-field coupling behavior and the heat and mass transfer mechanism in laser additive manufacturing process. In this study, a coupled thermal-fluid–solid multi-physical field numerical model for the laser cladding of 316L stainless steel powder on 45 steels was developed. The transient change patterns of the temperature, flow and stress fields for the cladding process were quantitatively revealed. The diffusion process of the powder elements within the molten pool was considered to reveal the element distribution law in the clad layer. The effects of the surface tension, buoyancy for molten pool, and Marangoni convection on the flow field also were considered, and the validity of the numerical model was verified. This study provides a theoretical basis for optimizing the laser cladding process.

Keywords Laser additive manufacturing · Multi-field coupling · Heat and mass transfer mechanism · Marangoni stream

1 Introduction

Laser cladding is an emerging green additive manufacturing technology with the high efficiency, accuracy and reliability, which can provide coatings with excellent quality for various materials. It has the advantages of the great metallurgical bonding performance, high powder utilization rate, small heat input to the workpiece, low dilution rate, and green energy saving. It is widely used in the metal material processing, medical device manufacturing, power industry, energy exploration, and other fields[1–3]. The quality of the cladding layer directly determines the service life for the metal part. It is important to conduct an in-depth study for the melting process on the multi-field coupled transient evolution mechanism and the elemental diffusion behavior of the molten powder material.

In recent years, a large amount of research on the mechanism for laser cladding process has been conducted by domestic and foreign researchers. In 2008, Huang Y L [4] investigated the concentration distribution of the molten component and the junction coupling for the substrate components. The distribution coefficient of non-equilibrium solute and the distribution for Fe element were calculated, and the results were in agreement with the expectation. In 2011, Fallah V [5] simulated the transient change pattern of molten pool morphology during laser deposition using the birth–death cell method. The deposition of Ti45Nb on Ti-6Al-4 V substrate was simulated by the continuous transformation of the cladding layer for the "birth" unit into the "death" unit during the cladding. And the model calculation results accorded with the experimental results. In 2012, Hu Y W [6] established a numerical simulation of spot welding process for stainless steel-nickel heterogeneous material. The influence of heat and mass transfer on the molten pool flow was analyzed, and the convection effect was explored. The results show that molten pool convection affects the heat and mass transfer behavior in the welding process. In 2017,

Recommended for publication by Commission I—Additive Manufacturing, Surfacing, and Thermal Cutting.

✉ Chang Li
lichang2323-23@163.com

[1] School of Mechanical Engineering and Automation, University of Science and Technology Liaoning, Anshan 114051, Liaoning, China

Gan Z T [7] developed a numerical model for the heat and mass transfer in laser cladding process based on the multi-field coupling method. The material transfer of the cladding process was analyzed. And the validity of the numerical model was verified by comparing the numerical calculation results for the molten layer profile with the experimental results. However, there is a 17% error in the distribution of Co elements in this study, mainly due to that the numerical model ignores the influence on thermal physical parameters of the substrate and powder materials by the temperature. In 2018, Wirth F [8] developed a three-dimensional numerical model of the coaxial laser cladding process. The modeling process considered factors such as the heat transfer, fluid flow, and surface tension. In 2019, Li C [9] analyzed the variation of the coupled thermal-elastic–plastic-fluidic multi-field in the laser cladding process. The mechanism of multi-physics field coupled transient evolution was revealed, and the model accuracy was also verified by experiments. In 2019, Song B X [10] analyzed the transient evolution law inside the molten pool by building a numerical model of laser cladding. Studies showed that there is a circular convection inside the molten pool, with molten metal flowing from the pool bottom to the surface and liquid metal on the surface flowing back to the bottom along the sides of the pool. In 2019, Liu H [11] developed a numerical model of laser cladding using a wide beam, which studied the evolution of the temperature field in the cladding process. The interrelationships among the temperature gradient G, cooling rate ε, and solidification rate R were analyzed, and the microstructure of the cladding layer was investigated. The results showed that the cooling rate of the cladding layer gradually decreases after the laser sweep, and the G/R shows a trend of decreasing and then increasing.

At present, most of the studies are on the temperature and flow fields in the cladding process, and there are few studies on the transient changes of thermal stresses in the cladding process. This study established a numerical model of the laser cladding process, which coupled the heat-flow-solid multi-physical fields and quantitatively revealed the changes of the temperature, flow and stress fields in the cladding process. The study lays an important theoretical foundation for further improving the cladding quality and optimizing the process parameters.

2 Finite element model and theoretical basis

The theoretical model is based on the following assumptions:

(1) The laser power is constant and the energy density is Gaussian distributed.
(2) The fluid is laminar and incompressible.
(3) The material is isotropic.
(4) The clad material meets the von-Mises yield criterion.

2.1 Control equations

The melting process involves temperature and fluid changes, and the controlling equations are as in Eq. (1) to Eq. (5) [12–14].

where Eq. (1) is the continuous mass equation, which are expressed as

$$\frac{\partial \rho}{\partial t} + \nabla \cdot (\rho \boldsymbol{u}) = 0 \tag{1}$$

where ρ is the material density, measured in kilogram per cubic meter (kg/m^3), t is the working time, measured in seconds (s), ∇ is the Hamiltonian, and $\boldsymbol{u}$ is the molten metal flow rate, measured in cubic meters per second (m^3/s).

The energy equation is shown as follows. The first term on the left side of Eq. (3) indicates heat accumulation, and the second term indicates heat convection. The first term on the right-hand side of the equation represents heat conduction, which are expressed as

$$\rho C_p \frac{\partial T}{\partial t} + \rho C_p \boldsymbol{u} \cdot \nabla T = \nabla \cdot (h \nabla T) - \frac{\partial H}{\partial t} - \rho \boldsymbol{u} \cdot \Delta H \tag{2}$$

where T is the working temperature, measured in kelvin (K); C_p is the material specific heat capacity, measured in joule per kilogram per kelvin ($J/(kg{\cdot}K)$); h is the thermal conductivity, measured in watt per meter per kelvin ($W/(m{\cdot}K)$); and ΔH is the latent heat of melting, measured in joule per kilogram (J/kg). Among them, the latent enthalpy expression is

$$\Delta H = L f_l \tag{3}$$

where L is the latent heat, measured in joule per kilogram (J/kg) and f_l is the mass fraction of molten metal, and the expression is

$$f_l = \begin{cases} 1, T > T_l \\ \frac{T - T_s}{T_l - T_s}, T_s \le T \le T_l \\ 0, T < T_s \end{cases} \tag{4}$$

where T_s is the solid-phase line temperature measured in kelvin (K) and T_l is the liquid phase line temperature, measured in kelvin (K).

The N-S momentum equation is shown as follows. The left side of Eq. (5) represents the inertial force, the first term on the right side represents the pressure, the second term represents the viscous force, and the last term represents the momentum dissipation in the solid–liquid mixing zone, which can be quantified according to the Carman-Kozeny equation, which are expressed as

$$\rho\left[\frac{\partial \boldsymbol{u}}{\partial t}+(\boldsymbol{u}\cdot\nabla)\boldsymbol{u}\right]=\nabla\cdot\left[-p\boldsymbol{I}+\mu\left(\nabla\boldsymbol{u}+(\nabla\boldsymbol{u})^{T}\right)-\frac{2\mu}{3}(\nabla\cdot\boldsymbol{u})\boldsymbol{I}\right]-\mathrm{K}_0\frac{(1-f_l)^2}{f_l^3+B}\boldsymbol{u} \tag{5}$$

where μ is the molten metal viscosity, measured in pascal-second ($Pa{\cdot}s$) p is the liquid pressure, measured in pascal (Pa) K_0 is the morphological correlation constant of the porous medium during the melting, and B is a very small number.

The stress equation is shown as follows, which are expressed as

$$\rho\frac{\partial \xi^2}{\partial t^2}=\nabla\cdot S+F_V \tag{6}$$

where ξ is the displacement, measured in meter (m); S is the stress, measured in pascal (Pa); and F_V is the body force for deformation measured in newton (N).

The absorption rate of laser energy by the substrate is not only influenced by the laser properties, but also related to the substrate properties. The interaction is given by the Hagen-Rubens equation, with the expression [15]

$$\alpha=\frac{2}{\sqrt{30}}\times\sqrt{\frac{r_e}{\lambda_0}} \tag{7}$$

where α is the absorption rate of the laser by the substrate, r_e is the material resistivity, measured in ohm-meter ($\Omega{\cdot}m$), and λ_0 is the laser wavelength measured in meter (m).

The degree of mixing of the substrate material with the cladding material affects the physical parameters of the cladding pool, which are expressed as

$$W_{mix}=\beta W_s+(1-\beta)W_p \tag{8}$$

where W_{mix} is the molten pool physical property parameter; W_s and W_p are the physical property parameters of substrate and cladding, respectively; and β is the mixing fraction, mainly the mass fraction of Fe elements.

2.2 Source terms and boundary conditions

During the melting, the laser heat source is a Gaussian heat source, and its expression is

$$q=\frac{2aP}{\pi R^2}exp\left(-\frac{2\left((x-vt)^2+y^2\right)}{R^2}\right) \tag{9}$$

where P is the laser power, measured in watts (W); a is the energy absorption rate; R is the laser radius, measured in meters (m); v is the scanning speed, measured in meters (m/s); x and y are the positions of the spot centers in the Cartesian coordinate system, measured in meters (m).

Heat exchange and heat radiation occur between the matrix and the surrounding environment, and the expression is

$$q_c=-h_c\left(T-T_0\right)-\sigma_b\varepsilon\left(T^4-T_0^4\right) \tag{10}$$

where h_c is the heat transfer coefficient, measured in watt per square meter per kelvin ($W/(m^2{\cdot}K)$; ε is the emissivity of the substrate surface; σ_b is the Stefan-Boltzmann constant, measured in watt per square meter per kelvin to the fourth power ($W/(m^2{\cdot}K^4)$); and T_0 is the initial temperature, 293.15 K. The molten pool surface is the gas/liquid interface, and the boundary condition is the momentum equation with the expression [16]

$$F_{L/G}=\sigma\boldsymbol{n}^*\kappa-\nabla_s T\frac{d\sigma}{dT} \tag{11}$$

where σ is the molten pool surface tension, measured in newton per meter (N/m), $\boldsymbol{n}^*$ is the molten pool surface normal vector, and κ is the molten pool surface curvature, measured in per meter (m^{-1}).

The coaxially fed powder laser melting process takes into account the molten pool gas/liquid interface motion, and the molten pool movement velocity is expressed as [17]

$$V_{L/G}=\boldsymbol{u}\cdot\boldsymbol{n}^*+\boldsymbol{V_p}\cdot\boldsymbol{n}^* \tag{12}$$

where $\boldsymbol{u}$ is the molten pool flow rate measured in meter per second (m/s) and $\boldsymbol{V_p}$ is the gas/liquid interface excursion velocity, measured in meter per second (m/s), which is expressed as [18]

$$\boldsymbol{V_p}=\frac{2m_f\eta_m}{\rho_m\pi R^2}exp\left(\frac{-2\left((x-Vt)^2+y^2\right)}{R_p^2}\right)\boldsymbol{z} \tag{13}$$

Table 1 45 steel materials composition (wt%)

C	Cr	Ni	Mn	P	S	Si	Fe
0.42–0.50	≤0.25	≤0.25	0.50–0.80	≤0.035	≤0.035	0.17–0.37	Residual

Table 2 316L materials composition (wt%)

C	Cr	Ni	Mn	P	S	Mo	Si	Fe
≤0.030	16.0–18.0	12.0–15.0	≤2.0	≤0.035	≤0.030	2.0–3.0	≤1.0	Residual

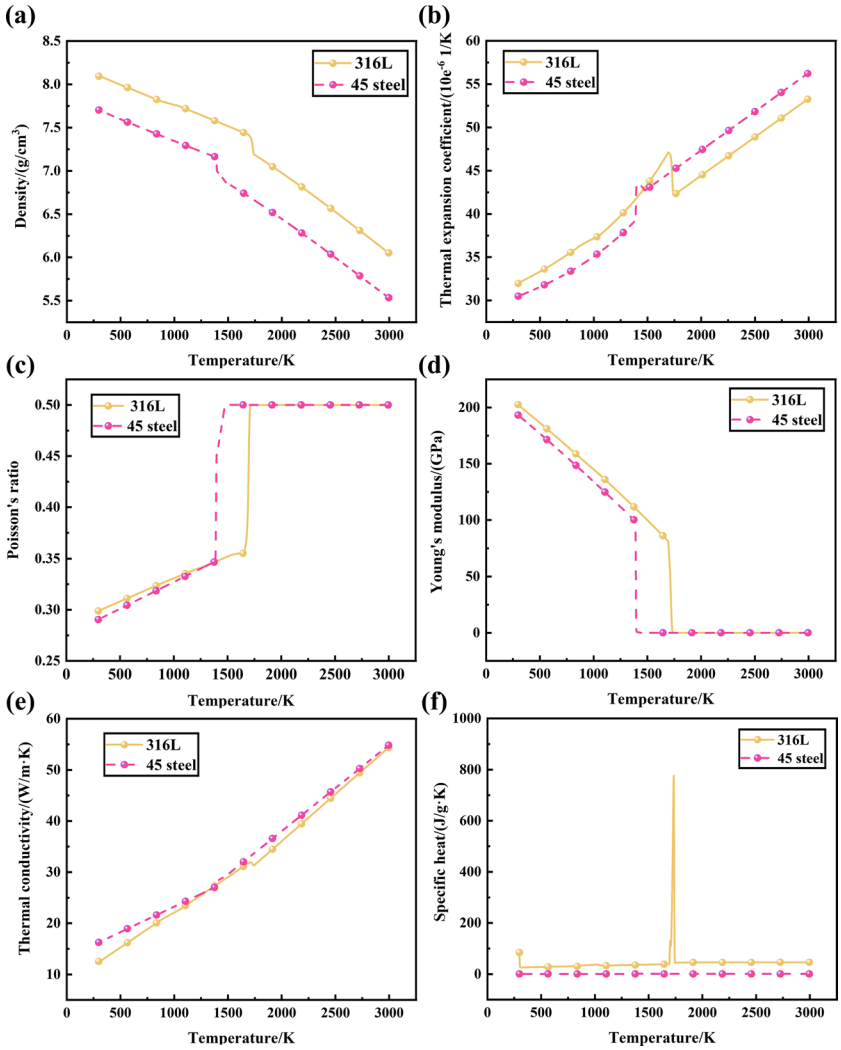

Fig. 1 Thermophysical property parameter curve: **a** density, **b** coefficient of thermal expansion, **c** Poisson's ratio, **d** Young's modulus, **e** thermal conductivity, **f** specific heat capacity

Table 3 Cladding process parameters

Process parameters	Value
Laser power (W)	700,850,1000
Scanning speed (mm/s)	6
Spot radius (mm)	3
Surface emissivity (1)	0.8
Boltzmann constant ($W•m^{-2}•K^{-1}$)	5.67×10^{8}
Convective heat transfer coefficient ($W•m^{2}•K^{-1}$)	100
Environment temperature (K)	293.15
Laser absorptivity (1)	0.8

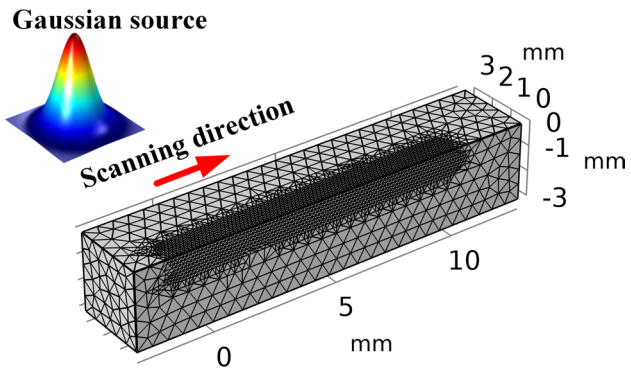

Fig. 2 Geometric model and meshing

where m_f is the amount of powder delivered, measured in kilogram (kg); η_m is the powder particle pooling efficiency; ρ_m is the powder material density, measured in kilogram per cubic meter (kg/m^3); R_p is the powder flow radius, measured in meter (m); and z is the unit vector in z direction.

During the laser cladding, when the powder passes through the laser beam, the powder particles absorb some of the laser energy, while the remaining energy acts on the substrate surface. The temperature of the powder

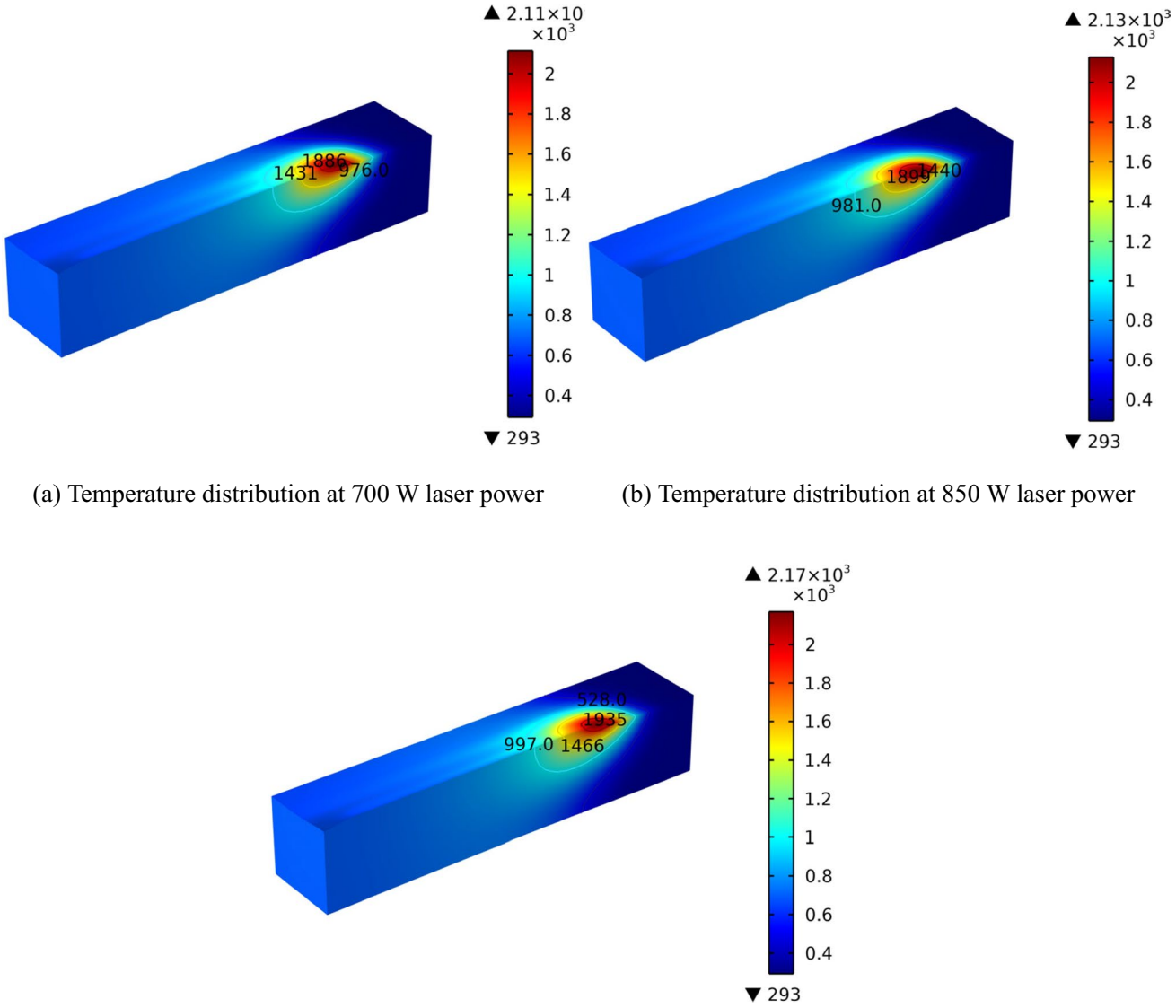

(a) Temperature distribution at 700 W laser power

(b) Temperature distribution at 850 W laser power

(c) Temperature distribution at 1000 W laser power

Fig. 3 Distribution of molten pool temperature under different laser powers

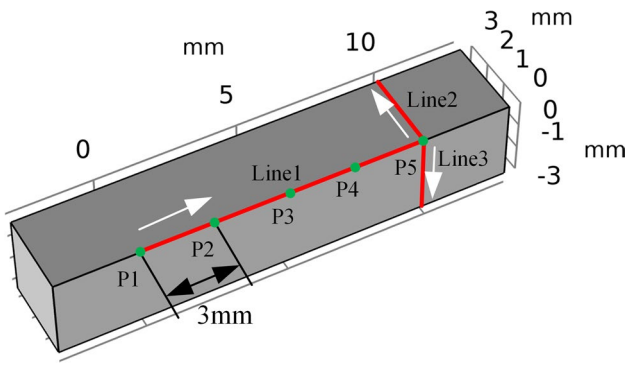

Fig. 4 Extract data location distribution

particles increases before entering the molten pool due to the absorption of laser energy [19–21]. According to Lambert–Beer light transmission theorem and Mie theory, the powder stream has an attenuating effect on the laser energy, the effect is related to the laser power, laser wavelength, powder properties, and powder stream concentration, and the expression is

$$q\prime(r,\phi) = qexp(-\delta N\phi) \tag{14}$$

where $q'(r, \phi)$ is the power density ϕ of the laser at a distance of nozzle center point r, q is the equivalent heat flux, measured in watt per square meter (W/m^2), δ is the absorption

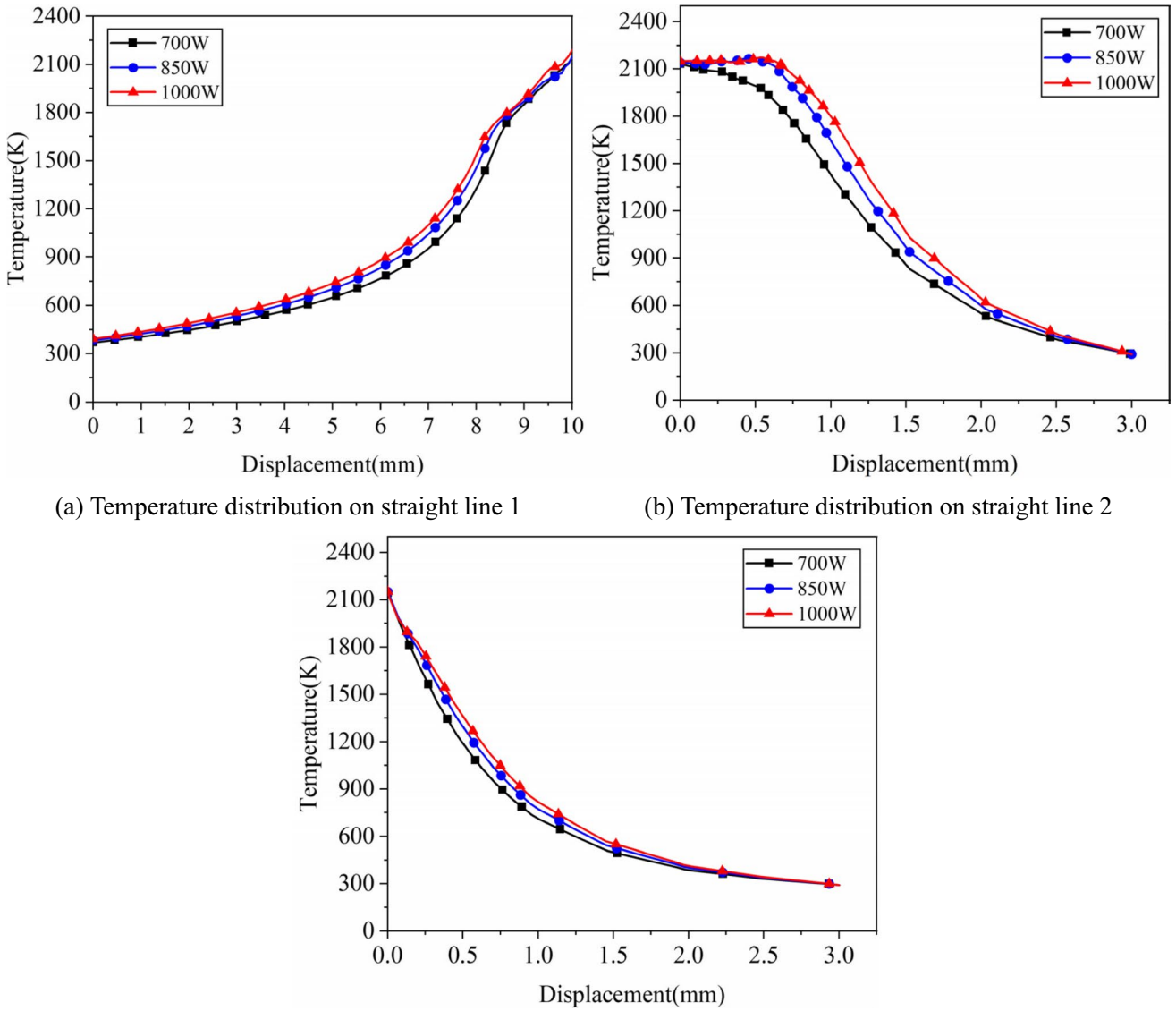

(a) Temperature distribution on straight line 1

(b) Temperature distribution on straight line 2

(c) Temperature distribution on straight line 3

Fig. 5 Temperature variation curves at different positions at 1000 ms

rate of laser energy by the powder, and N is the number of powder particles in the unit volume.

The expression for the yield criterion of the melting process is [22]

$$\frac{\sqrt{2}}{2}\sqrt{\left(\sigma_1-\sigma_2\right)^2+\left(\sigma_2-\sigma_3\right)^2+\left(\sigma_3-\sigma_1\right)^2}\le\sigma_s \tag{15}$$

where σ_1, σ_2, and σ_3 are the principal stresses in different directions of x, y, and z, respectively, measured in pascal (Pa), and σ_s is the yield limit measured in pascal (Pa).

The cladding process involves a multi-alloy system, which requires consideration of the inter-diffusion and interaction of the individual components. The mass transfer equation of the multi-alloy system is

$$\rho\frac{\partial C_i}{\partial t}+\rho(\boldsymbol{u}\cdot\nabla)C_i=\nabla\cdot\left(\rho D_i^m\nabla C_i+\rho C_i D_i^m\frac{\nabla M_n}{M_n}\right)+S_c \tag{16}$$

$$S_c=\nabla\cdot\left(\rho D_i^m\nabla\left(C_l-C_i\right)\right)-\nabla\cdot\left(\rho f_s\nabla\left(C_l-C_s\right)\boldsymbol{u}\right) \tag{17}$$

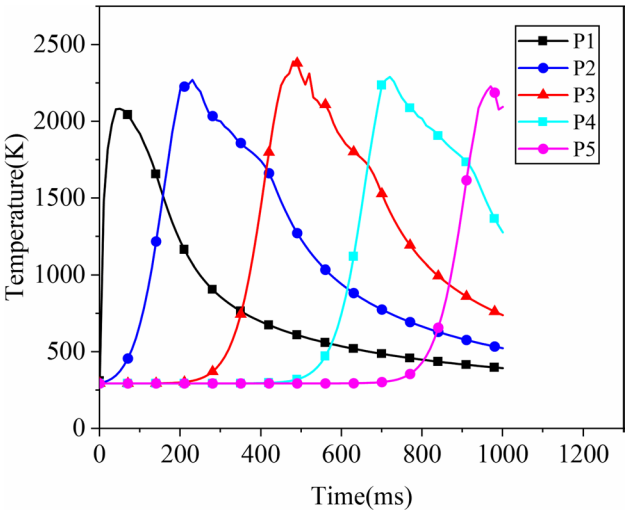

Fig. 6 Temperature varies with time at different points

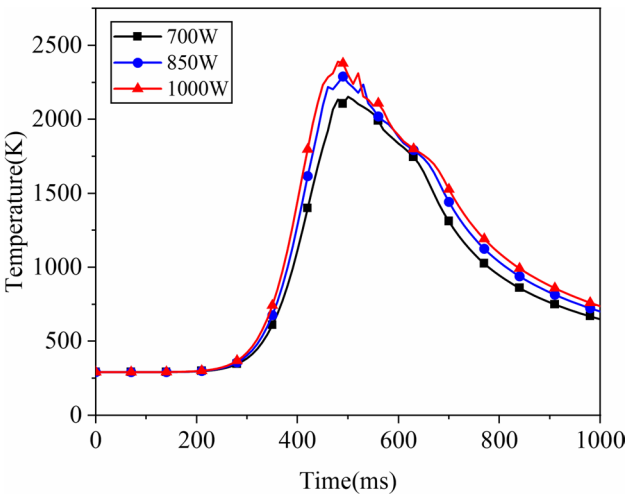

Fig. 7 Variation curve of melting temperature at P3

where C_i is the concentration of the ith component, measured in mole fraction (mol/mol), D_i^m is the average multicomponent mixing factor, and M_n is the average molar mass of the mixed components, measured in gram per mole (*g/mol*). In this case, the right-hand side of the equal sign of Eq. (16) is the multicomponent diffusion term, and the multicomponent diffusion mechanism is formulated using the mixed averaging method [23].

2.3 Laser cladding material, parameter selection, and geometric model

The cladding material is 316L stainless steel powder, and the substrate is 45 steel. 45 steel is a carbon structural steel, mainly containing carbon, silicon, and manganese, with high strength and moderate hardness, suitable for applications requiring strength and wear resistance; the element composition is shown in Table 1. 316L stainless steel is a kind of corrosion resistant stainless steel, mainly composed of chromium, nickel, and molybdenum, and has excellent corrosion resistance and oxidation resistance, suitable for high temperature environment; the element composition is shown in Table 2. The thermal property parameter curve of the material is shown in Fig. 1. The process parameters are shown in Table 3.

According to the characteristics of laser cladding forming, a 1/2 model is established, and the physical field is constrained by the symmetry surface. The geometric model and meshing are shown in Fig. 2.

The model as a whole is tetrahedrally meshed, with local refinement of the mesh for the fusion area. The model is meshed with a total of 68799 cells, 4368 boundary cells, and 209 edge cells. To effectively reflect the change in the geometry of the cladding layer during the melting, the laser

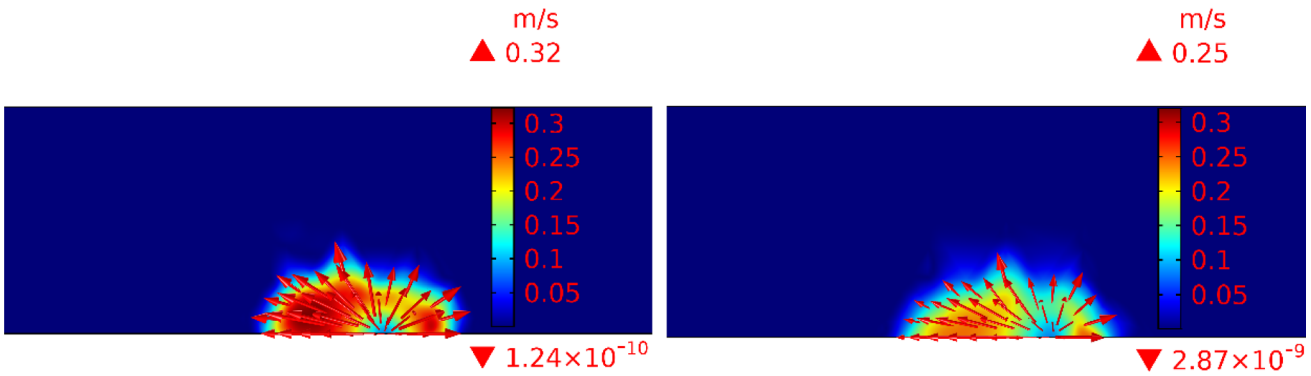

(a) Velocity distribution at 500 ms

(b) Velocity distribution at 1000 ms

Fig. 8 Velocity distribution at 700 W laser power

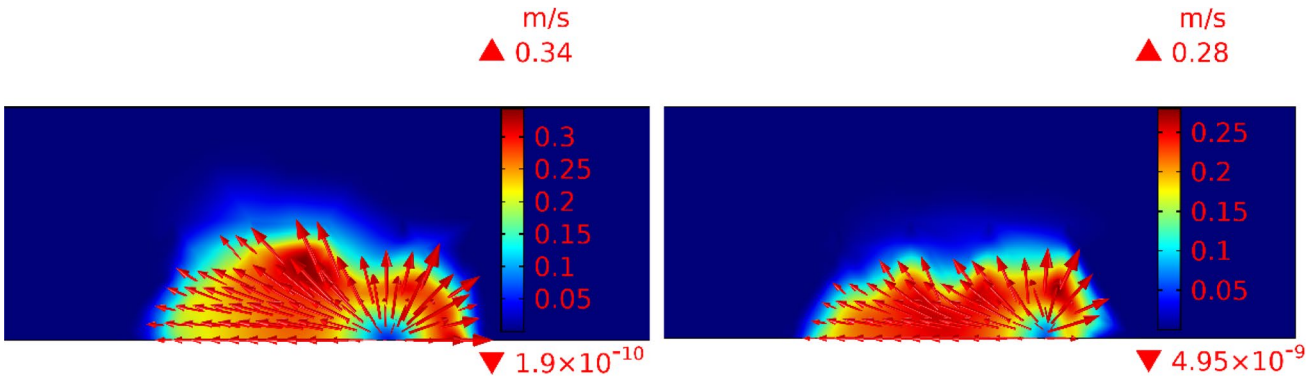

(a) Velocity distribution at 500 ms (b) Velocity distribution at 1000 ms

Fig. 9 Velocity distribution at 850 W laser power

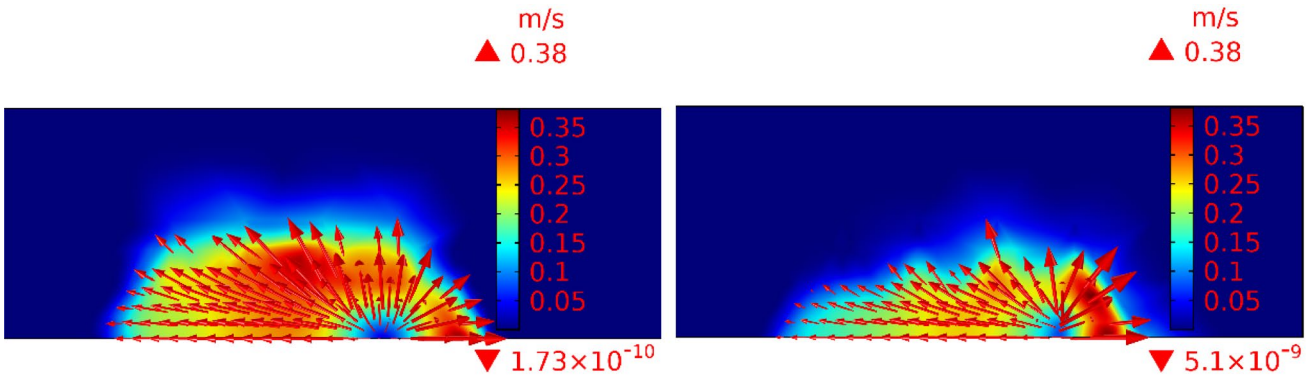

(a) Velocity distribution at 500 ms (b) Velocity distribution at 1000 ms

Fig. 10 Cloud map of molten pool flow rate distribution at laser power of 1000 W

cladding model is deformed using the deformation geometry technique.

3 Analysis of model calculation results

3.1 Analysis of temperature field results

The model is solved using a multi-field coupled numerical computation platform, and the computational results are analyzed.

During the melting, the temperature variation has a great influence on the molten pool size and the quality of the molten. The temperature field distribution clouds for different laser powers at 1000 ms are extracted and shown in Fig. 3. The figure shows that the molten pool is smaller at the laser power of 700 W. The highest temperature appears in the center of the molten pool at 2.24×10^3 K. The maximum molten pool temperature is 2.30×10^3 K at a laser power of 850 W. At a laser power of 1000 W, the molten pool increases slightly and the maximum molten pool temperature is 2.35×10^3 K. The calculation results show that as the laser power increases, the maximum molten pool temperature gradually increases, and the molten pool size gradually increases.

To accurately analyze the temperature change trend of the melting process, data are collected for acquisition lines 1, 2, 3 and acquisition points P1, P2, P3, P4, P5 in Fig. 4, and the calculated results are analyzed.

Figure 5 shows a graph of the temperature variation trend to the melting process at 1000 ms. Figure 5a shows the temperature variation curve on acquisition line 1. The figure shows that the temperature gradually increases as the collection line approaches the center of the molten pool, and the rate of temperature rise becomes faster with increasing distance. At 8 mm, the temperature inflection point occurs, and thereafter the temperature rises at almost the same rate. Figure 5b shows the temperature variation curve on line 2. The

Fig. 11 Flow of molten metal in the molten pool

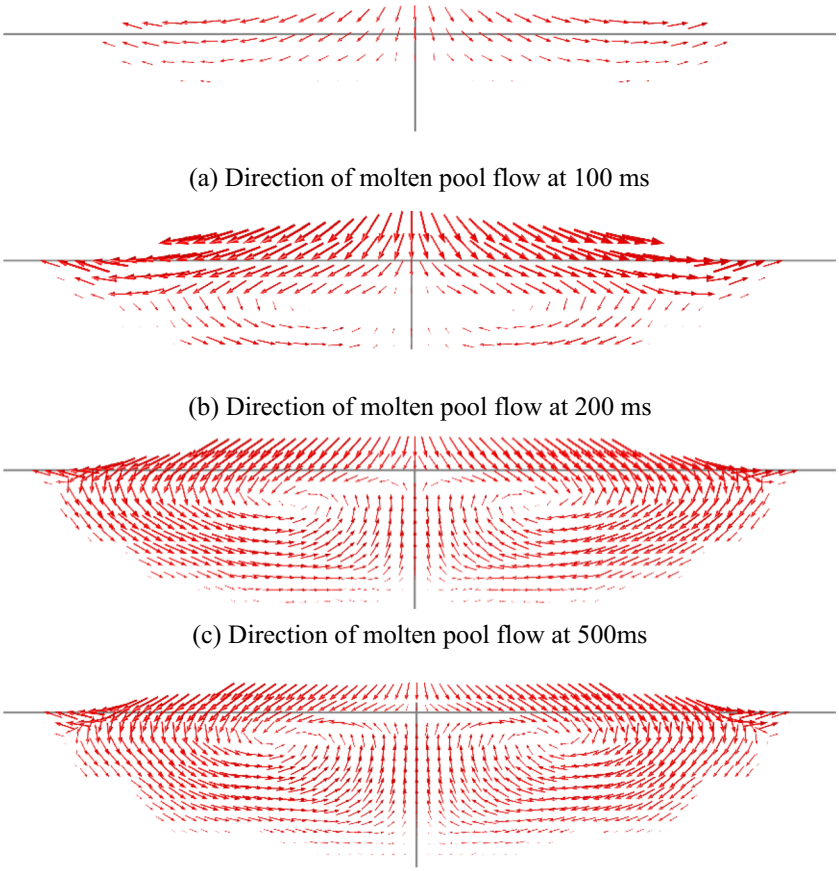

(a) Direction of molten pool flow at 100 ms

(b) Direction of molten pool flow at 200 ms

(c) Direction of molten pool flow at 500ms

(d) Direction of molten pool flow at 1000ms

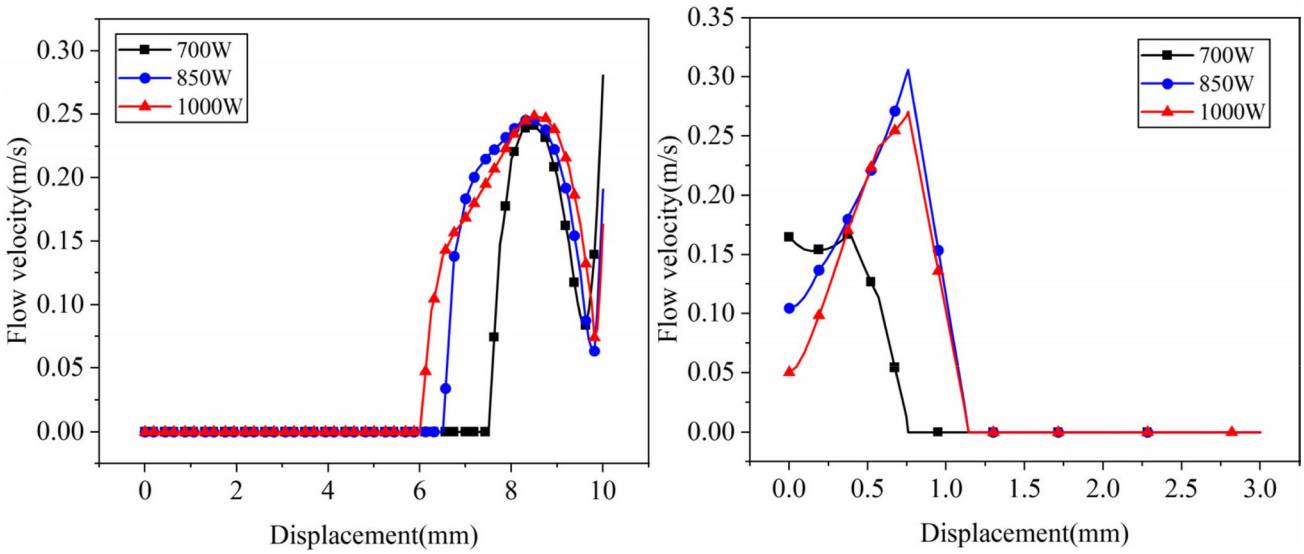

(a) Molten pool flow rate distribution on line 1

(b) Molten pool flow rate distribution on line 2

Fig. 12 Variation curve of molten pool flow rate at different positions

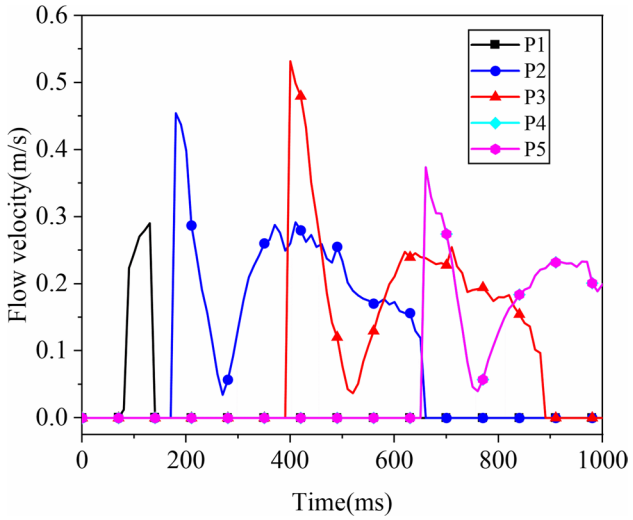

Fig. 13 Velocity changes with time at different points

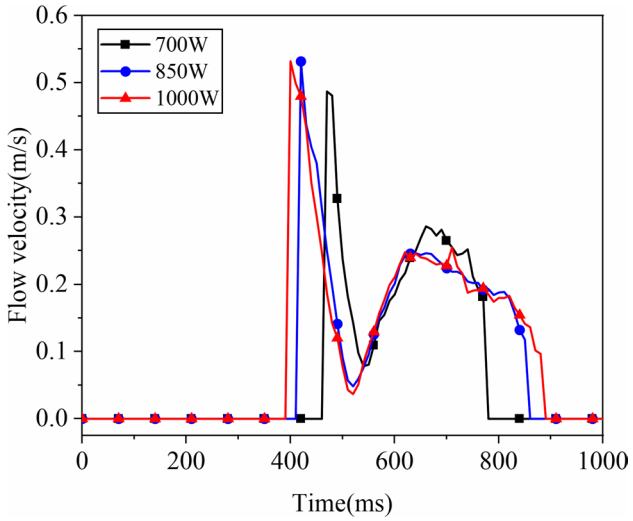

Fig. 14 Variation curve of melt pool flow rate at P3

graph shows that the temperature decreases as the distance increases. At 3 mm, the temperature was reduced to 300 K. It shows that the highest temperature of the cladding occurs in the center of the molten pool and the edge of the substrate is close to the ambient temperature. Figure 5c shows the temperature variation curve on line 3. The figure shows that the temperature gradually decreases with the increase of distance, and the decreasing speed gradually decreases. By comparing Fig. 5a, b, and c, it can be seen that the melting temperature is always the highest at laser power of 1000 W, followed by 850 W, while the melting temperature below 700 W is always the lowest.

The temperature variation curves of different acquisition points at the extraction power of 1000 W are shown in Fig. 6. The graph shows that the temperature change curve at P1 has the smallest peak. This is because P1 is at the beginning of the melting work, where the laser irradiation time is short, the absorbed energy is less, and the temperature is lower. The temperature variation at different acquisition points shows that the melting process ramps up faster and cools down slower after reaching the peak. This is because the warming is mainly influenced by the laser energy input, while the cooling is mainly influenced by the thermal convection and thermal radiation between the substrate and the environment.

The variation curve of the melting temperature at extraction P3 at different power is shown in Fig. 7. As can be seen from the figure, the temperature at P3 shows a trend of increasing and then decreasing, and the heating rate is greater than the cooling rate, and the melting temperature increases with the increase of laser power.

3.2 Analysis of flow field results

During the cladding, the molten metal flow is difficult to be observed experimentally, and numerical simulations are effective in bridging the research gap. The cloud map of molten pool flow rate distribution at 700 W laser power is extracted and shown in Fig. 8. The figure shows that the maximum molten pool flow rate is 0.32 m/s at 500 ms. The flow rate is radial on the surface of the molten pool. The maximum flow rate is 0.25 m/s at 1000 ms. Larger flow rate behind the molten pool and smaller molten pool size. The cloud map of the molten pool flow rate distribution at 800 W laser power is extracted and shown in Fig. 9. The maximum molten pool flow rate was 0.34 m/s at 500 ms. At 1000 ms, the maximum molten pool flow rate is 0.28 m/s. The molten pool size is larger compared to when the laser power is 700 W. The cloud map of the molten pool flow rate distribution at 1000 W laser power is extracted and shown in Fig. 10. At 500 ms, the maximum molten pool flow rate is 0.38 m/s. The maximum molten pool flow rate was also 0.38 m/s at 1000 ms. The molten pool flow rate increases at 1000 W, and the molten pool size is larger.

To further observe the internal flow state of the molten pool, a transverse section of the molten pool was performed along the Marangoni convection center. The extracted power is 1000 W at different moments of the flow direction cloud diagram, as shown in Fig. 11. From the figure, it can be seen that at 100 ms, the molten pool is not enough to form a complete Marangoni flow inside due to the short laser irradiation time. At 200 ms, the continuous input of laser energy, the surface tension of the molten pool gradually increases, and a Marangoni convection trend appears inside the molten pool. At 500 ms, the Marangoni effect is evident in the molten pool and a complete Marangoni convection is formed. The flow state of the molten metal at 1000 ms is similar to that at

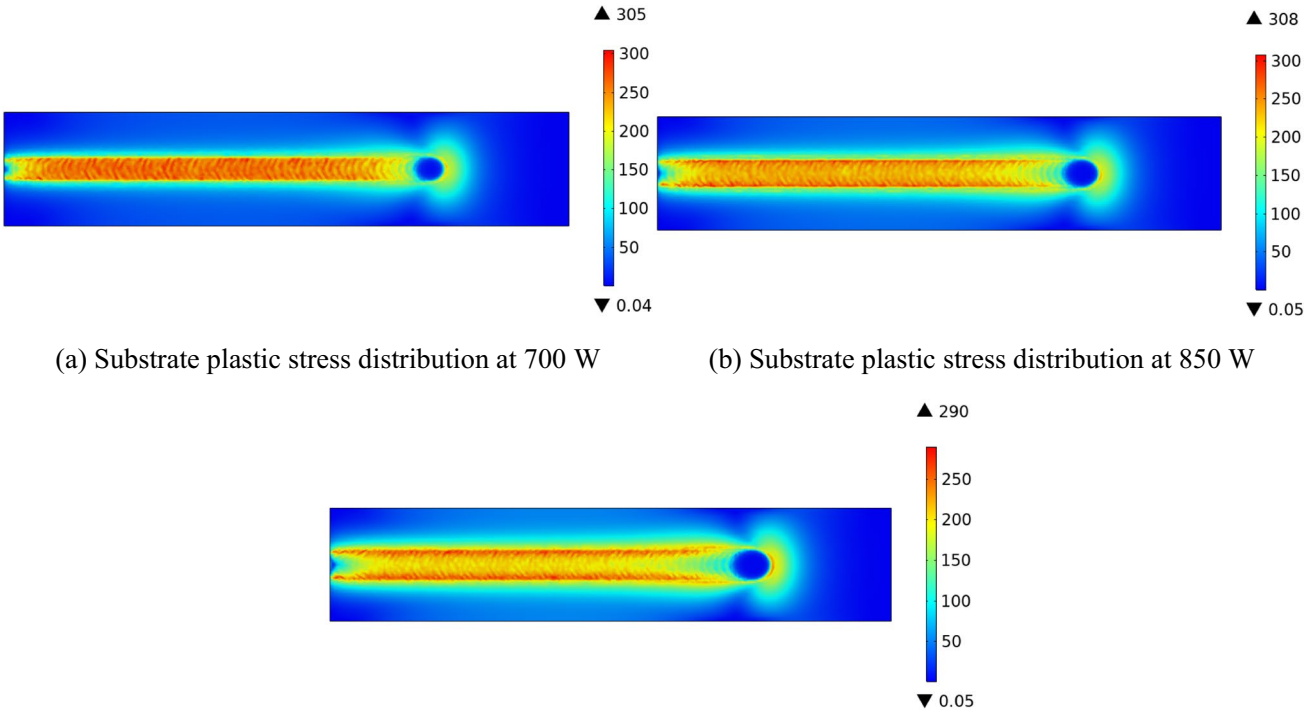

(a) Substrate plastic stress distribution at 700 W

(b) Substrate plastic stress distribution at 850 W

(c) Substrate plastic stress distribution at 1000 W

Fig. 15 Substrate plastic stress distribution under different laser powers

500 ms, indicating that the internal flow of the molten pool is stable from 500 to 1000 ms, all in the form of Marangoni flow.

The flow rate variation curves at different positions at 1000 ms are extracted and shown in Fig. 12. On the straight line 1, the molten pool flow rate shows a trend of increasing, then decreasing, and then increasing due to the Marangoni effect. The Marangoni convection center is at 10 mm and its flow velocity is low. Marangoni convection center positions at 0 mm on straight line 2. The figure shows that the Marangoni convective effect is strongest, and the flow velocity is lowest in the central region when the laser power is 1000 W. At 700 W, the Marangoni convection effect is weaker, and the flow velocity is higher in the central region. The molten pool flow rate gradually increases as it moves away from the Marangoni convection center. Gradually approaching the edge of the molten pool, the molten pool flow rate gradually decreases.

The variation curves of the molten pool flow rate at different positions at 1000 W are extracted and shown in Fig. 13. It can be seen in the figure that the Marangoni flow is not formed at P1 due to the short irradiation time by the laser, and the flow velocity is small. At P2, P3, P4, and P5, due to the longer laser irradiation time, an obvious Marangoni flow was formed inside the molten pool, and the molten pool flow rate showed two peaks, and the first peak was larger than the second peak.

The flow rate variation curves at P3 with different laser powers are extracted and shown in Fig. 14. As can be seen from the figure, the molten pool size is larger at 1000 W laser power, and the flow rate is not much different from that at 850 W. When the laser power is 1000 W, the flow rate in front of the molten pool is larger than that in the back, but the flow rate distribution in front of the molten pool is smaller. At different powers, the molten pool flow rate changes with time showing a trend of increasing, then decreasing, then increasing, and then decreasing. The first peak occurs when the maximum flow rate is at the front side of the molten pool. The second time the peak occurs when the molten pool flow rate distribution is located at the back side of the molten pool.

3.3 Analysis of stress field results

A cloud of plastic stress distribution at different powers at 1000 ms is extracted and shown in Fig. 15. The figure shows that the substrate plastic stress is mainly distributed on the laser scanning path. Due to the difference in physical parameters between the substrate and the clad material, the stresses are more concentrated on both sides of the clad channel.

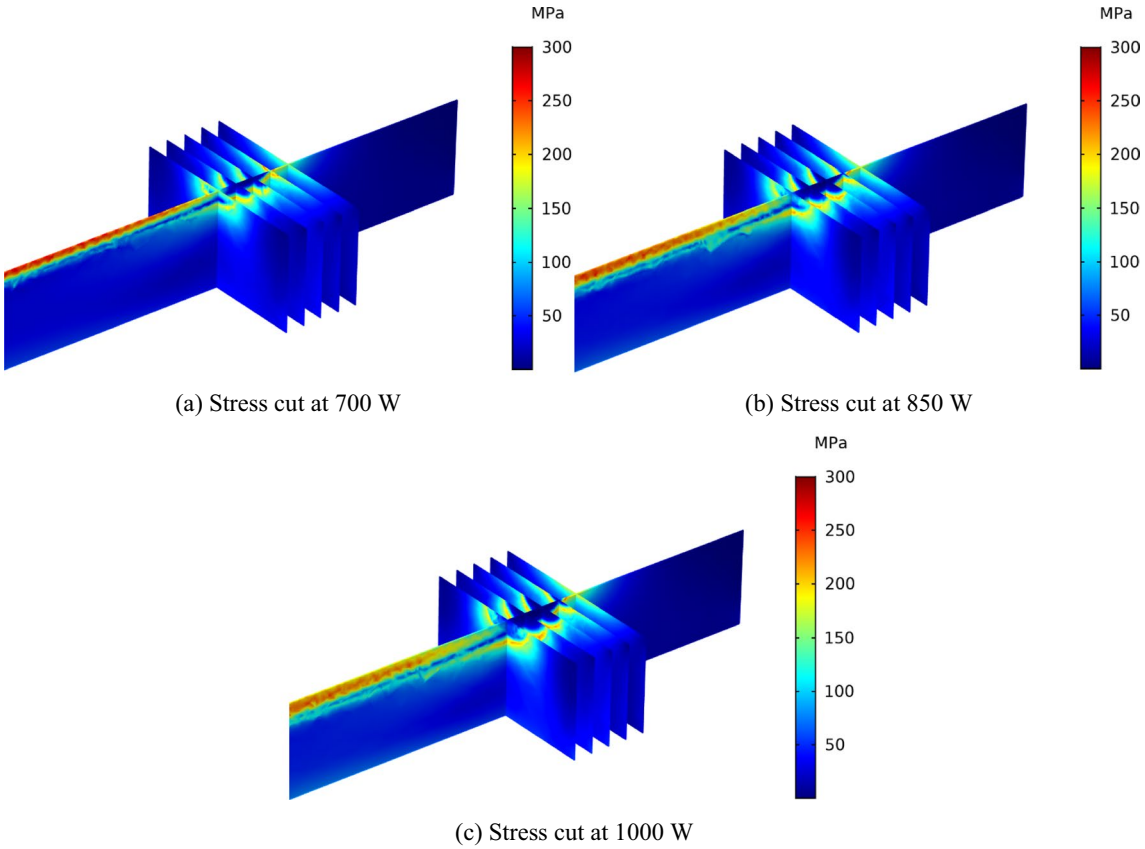

(a) Stress cut at 700 W

(b) Stress cut at 850 W

(c) Stress cut at 1000 W

Fig. 16 Stress section view under different laser powers

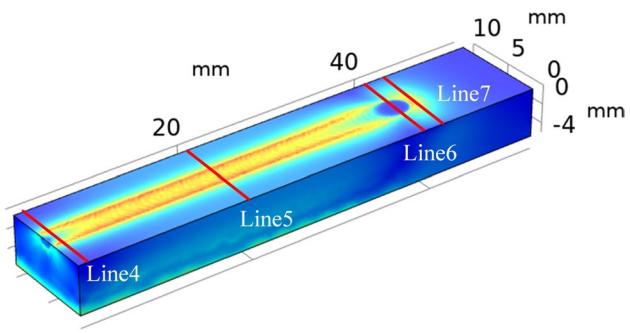

Fig. 17 Stress extraction location

In the laser irradiated region, the stress in the center of the molten pool is close to 0 MPa due to the solid and liquid phase change of the molten metal. In front of the molten pool, the plastic stress is ellipsoidally distributed due to the higher temperature. The maximum substrate plastic stress is 305 MPa at a laser power of 700 W. Due to the low laser power, the heat-affected zone formed is smaller, and the stress distribution is narrower. As the laser power increased to 850 W, the heat-affected zone formed increased, and the stress distribution became wider, with the maximum plastic stress reaching 308 MPa. The maximum plastic stress is 290 MPa at a laser power of 1000 W, and the plastic stress distribution range is relatively larger.

The stress distribution clouds of the cut surface around the molten pool at different laser powers are shown in Fig. 16. The figure shows that there is almost no stress inside the molten pool. Stress exists at the bottom of the molten pool, and the higher the laser power, the greater the stress range at the bottom of the molten pool. Less stress around the molten cladding layer compared to the area behind the scan.

To reveal the stress field change pattern during the melting, the line 4 to line 7 stress data were extracted, as shown in Fig. 17. In particular, line 4 is 1 mm from the left end of the workpiece, line 5 is 20 mm from the left end of the workpiece, line 6 passes through the center of the molten pool, and line 7 is 3 mm from the center of the molten pool.

The stress variation curve is extracted according to the collection line in Fig. 17, as shown in Fig. 18. The figure shows that the straight line 4 is located at the initial position with higher stresses on both sides of the molten channel and lower stresses near the middle. The peak of plastic stress is maximum at laser power of 1000 W. The stress peak is minimized at 700 W. In a straight line 5, the stress at the center

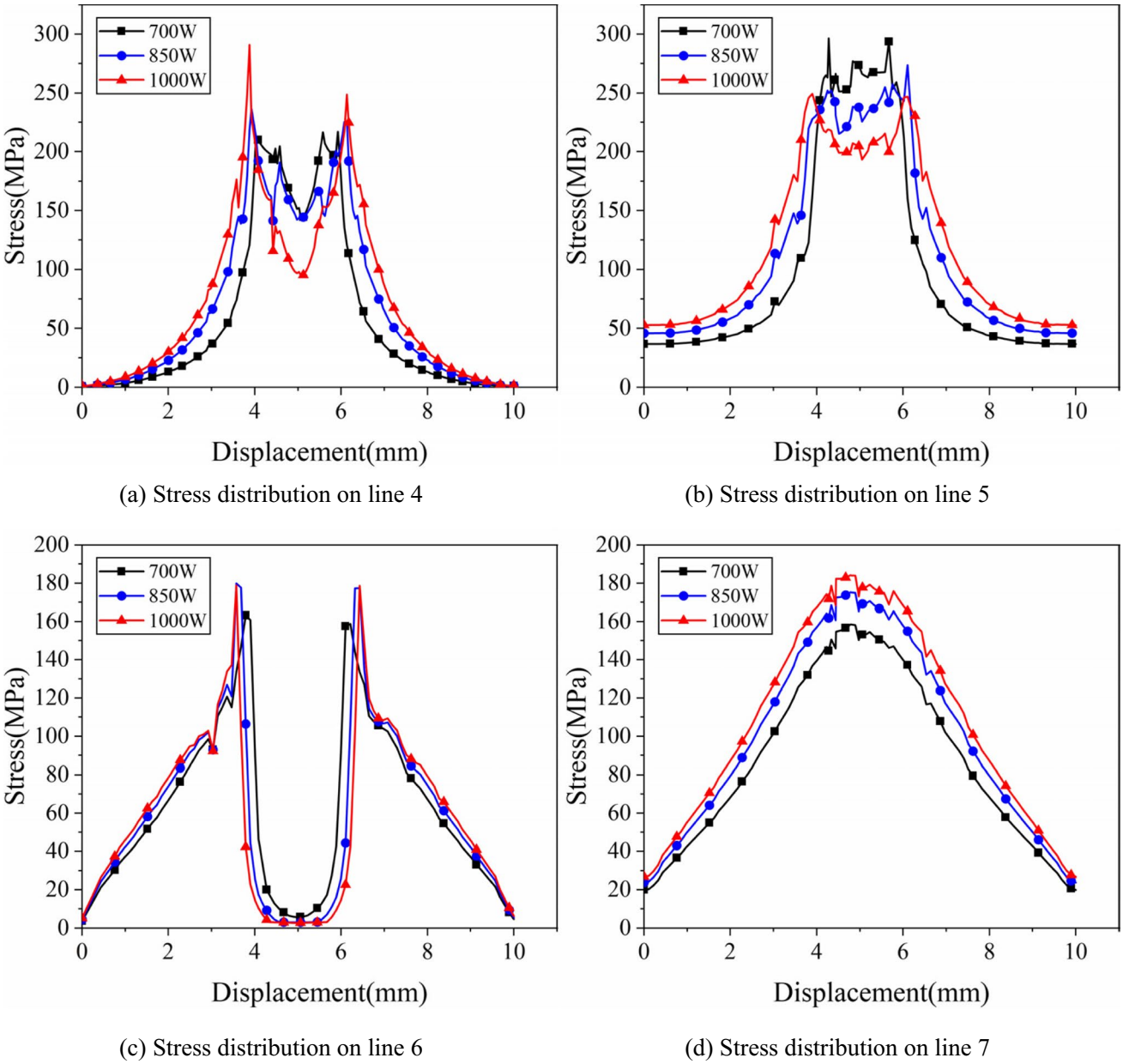

(a) Stress distribution on line 4

(b) Stress distribution on line 5

(c) Stress distribution on line 6

(d) Stress distribution on line 7

Fig. 18 Stress variation curve at different positions

of the fusion channel is slightly lower than at the sides. The stress distribution generated at 1000 W has a large range, and at 700 W, the stress distribution is relatively small. Since the straight line 6 passes through the center of the molten pool, less stress is generated inside the molten pool. As the laser power increases, the stress inside the molten pool tends to decrease. Straight line 7 is located in front of the molten pool, and the plastic stress shows a trend of increasing and then decreasing. The plastic stress was maximum with a peak value of 179.26 MPa at 1000 W laser power and minimum at 150.33 MPa at 700 W laser power.

3.4 Analysis of elemental distribution results

The distribution clouds of Fe, C, Cr, and Ni elements in the molten layer at the laser power of 1000 W are shown in Fig. 19. Figure 19a shows that the initial content of elemental Fe in the substrate is 98%. At the initial stage of cladding, the molten pool is not fully formed, the molten pool flow rate is small, and the 316L powder material in the molten pool is not fully mixed with the base material, resulting in the elemental Fe content in this area close to the elemental Fe content in the base. As the cladding work

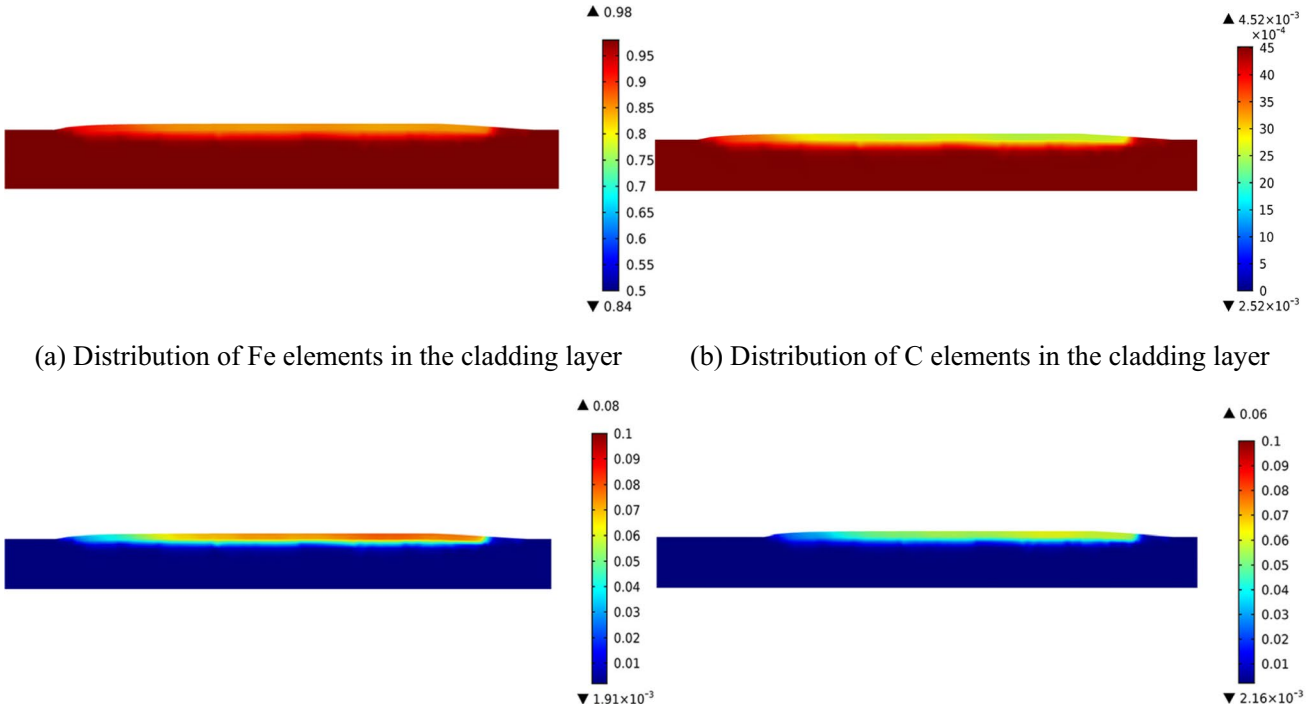

(a) Distribution of Fe elements in the cladding layer

(b) Distribution of C elements in the cladding layer

(c) Distribution of Cr elements in the cladding layer

(d) Distribution of Ni elements in the molten layer

Fig. 19 Concentration of Fe, C, Cr, and Ni elements

proceeds, the molten metal flows fully under the influence of Marangoni effect, and the 316L powder material is fully mixed with the base material, when the minimum value of Fe element content is 84%. Figure 19b shows that the base material is 45 steel with an initial element C content of 0.45%. In the initial stage of cladding, the C element content is close to the substrate. As the cladding work proceeds, there is a decreasing trend of C element content in the clad layer. After the molten pool is stabilized, the minimum content of element C in the clad layer is 0.252%. Figure 19c shows that the initial content of elemental Cr in the substrate is 0.25%, and the content of elemental Cr in the molten powder is 16%. At the initial stage of cladding, the Cr element content did not change significantly. As the cladding work proceeds, the Cr element content gradually increases to a maximum of 8%. Figure 19d shows that the initial content of elemental Ni in the substrate is 0.25%, and the content of elemental Ni in the molten powder is 12%. The maximum content of Ni element in the clad layer is up to 6%.

The cloud plot of Fe element concentration distribution on the molten surface at different moments when the laser power is 1000 W is shown in Fig. 20. It can be seen in the figure that at 100 ms, due to the short laser irradiation time, the molten pool formed is smaller, and the molten metal flows slower, so the Fe element concentration changes less, from 98 to 93%. At 200 ms, the laser energy is continuously fed, the molten pool becomes larger, and the minimum Fe element concentration decreases to 90%. At 300 ms, the molten pool stabilized and the minimum value of Fe element concentration was 86%. The minimum value of Fe element concentration in the molten layer is 84% at 500 ms. At this point, it is the same as the minimum value of Fe element concentration at 700 ms and 1000 ms. The calculation shows that the trend of Fe concentration in the clad layer changes from gradually decreasing to stabilizing as the cladding work proceeds. The concentration of elemental Fe is lower in the center of the molten pool and behind the molten pool due to Marangoni convection.

The cloud plot of C element concentration distribution on the surface of the molten layer at different moments when the laser power is 1000 W is shown in Fig. 21. The graph shows that the element C concentration decreases from 0.451 to 0.383% at 100 ms. At this time, the molten pool is not fully formed, and the molten metal does not have solidification behavior. At 200 ms, the molten pool was expanded due to the continuous laser irradiation, and the lowest value of C element concentration was 0.344%. At 300 ms, the elemental C concentration was further reduced to a minimum value

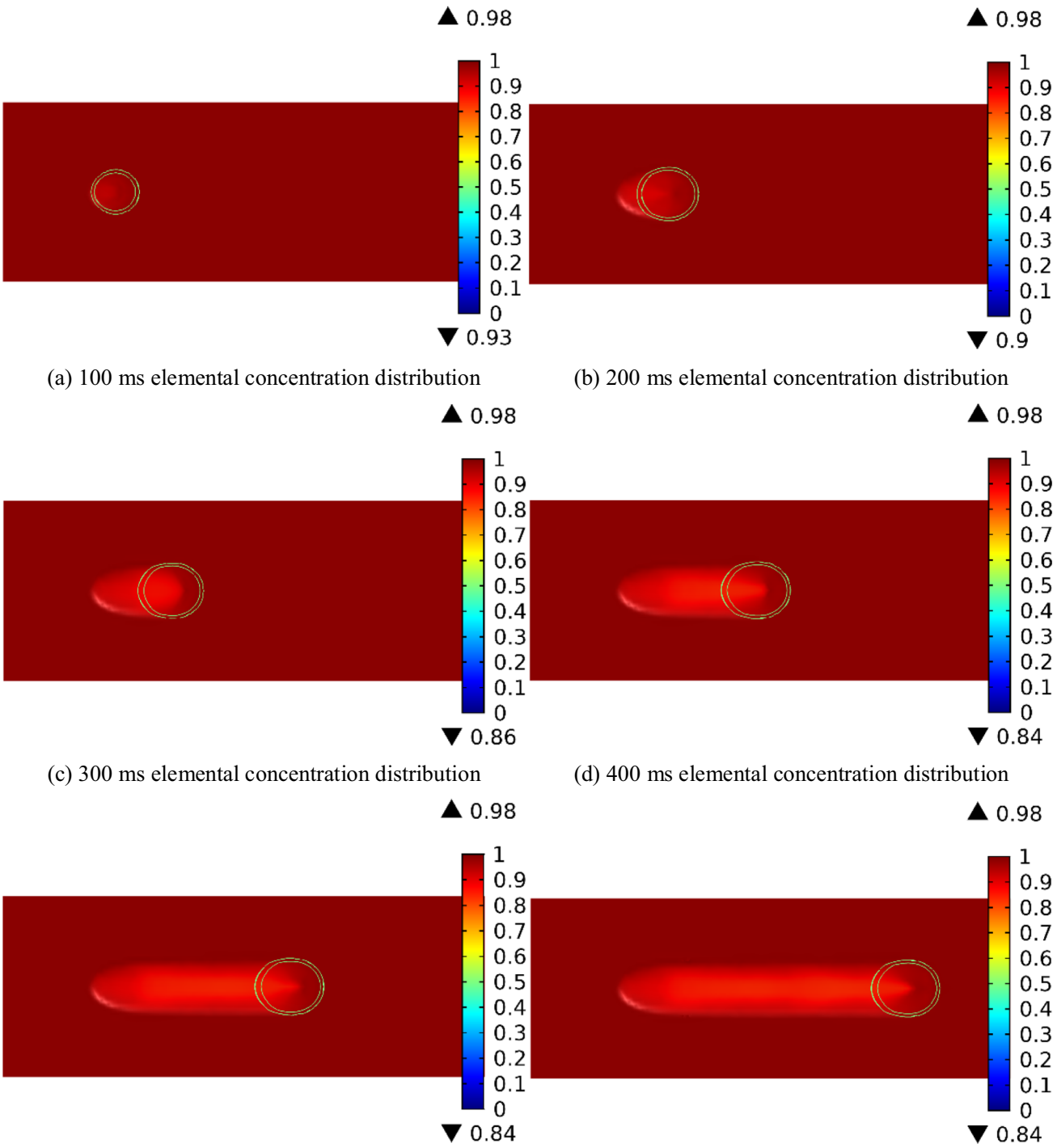

(a) 100 ms elemental concentration distribution

(b) 200 ms elemental concentration distribution

(c) 300 ms elemental concentration distribution

(d) 400 ms elemental concentration distribution

(e) 700 ms elemental concentration distribution

(f) 1000 ms elemental concentration distribution

Fig. 20 Cloud map of Fe concentration distribution at different moments

of 0.298%. At 500 ms, the melting process reaches a steady state with a minimum value of 0.264% C element concentration, which is less different from the C element content at 700 ms and 1000 ms.

The cloud plot of Cr element concentration distribution on the surface of the molten layer at different moments when the laser power is 1000 W is shown in Fig. 22. The figure shows that the elemental Cr content is 3% at 100 ms, at

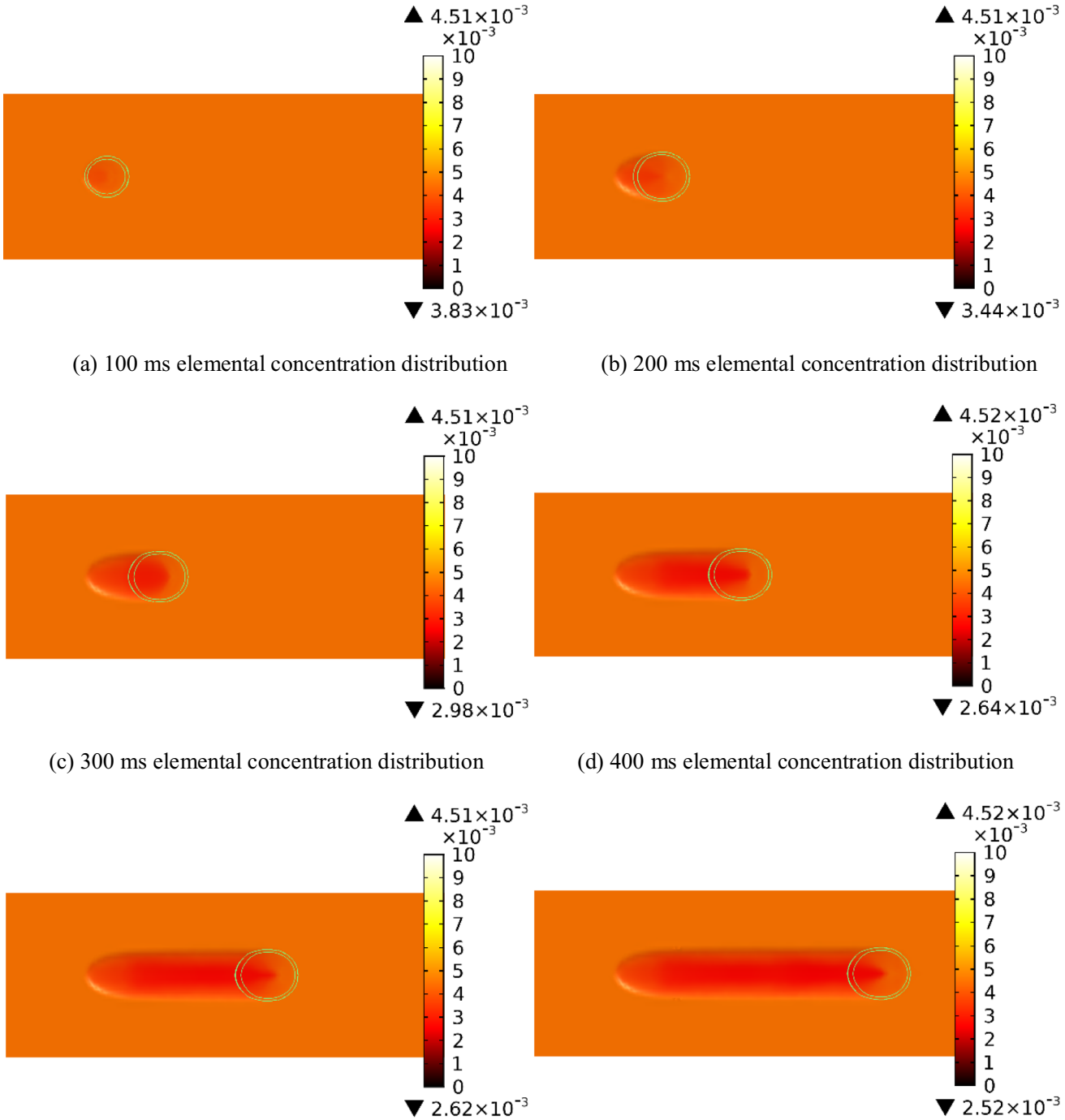

(a) 100 ms elemental concentration distribution

(b) 200 ms elemental concentration distribution

(c) 300 ms elemental concentration distribution

(d) 400 ms elemental concentration distribution

(e) 700 ms elemental concentration distribution

(f) 1000 ms elemental concentration distribution

Fig. 21 Cloud map of C concentration distribution at different moments

the initial stage of melting and cladding. At 200 ms, the molten pool was initially formed, and the elemental Cr content increased to 4%. At 300 ms, the molten pool is fully formed, and the elemental Cr content increases to 6%. At 500 ms, the molten pool gradually increased, and the maximum Cr element concentration reached 7%. In contrast, the maximum value of Cr element concentration varied less from 500 to 1000 ms. Calculations show that the Cr element in the clad layer shows a gradual increase as the cladding work proceeds.

The cloud plot of Ni element concentration distribution on the surface of the molten layer at different moments

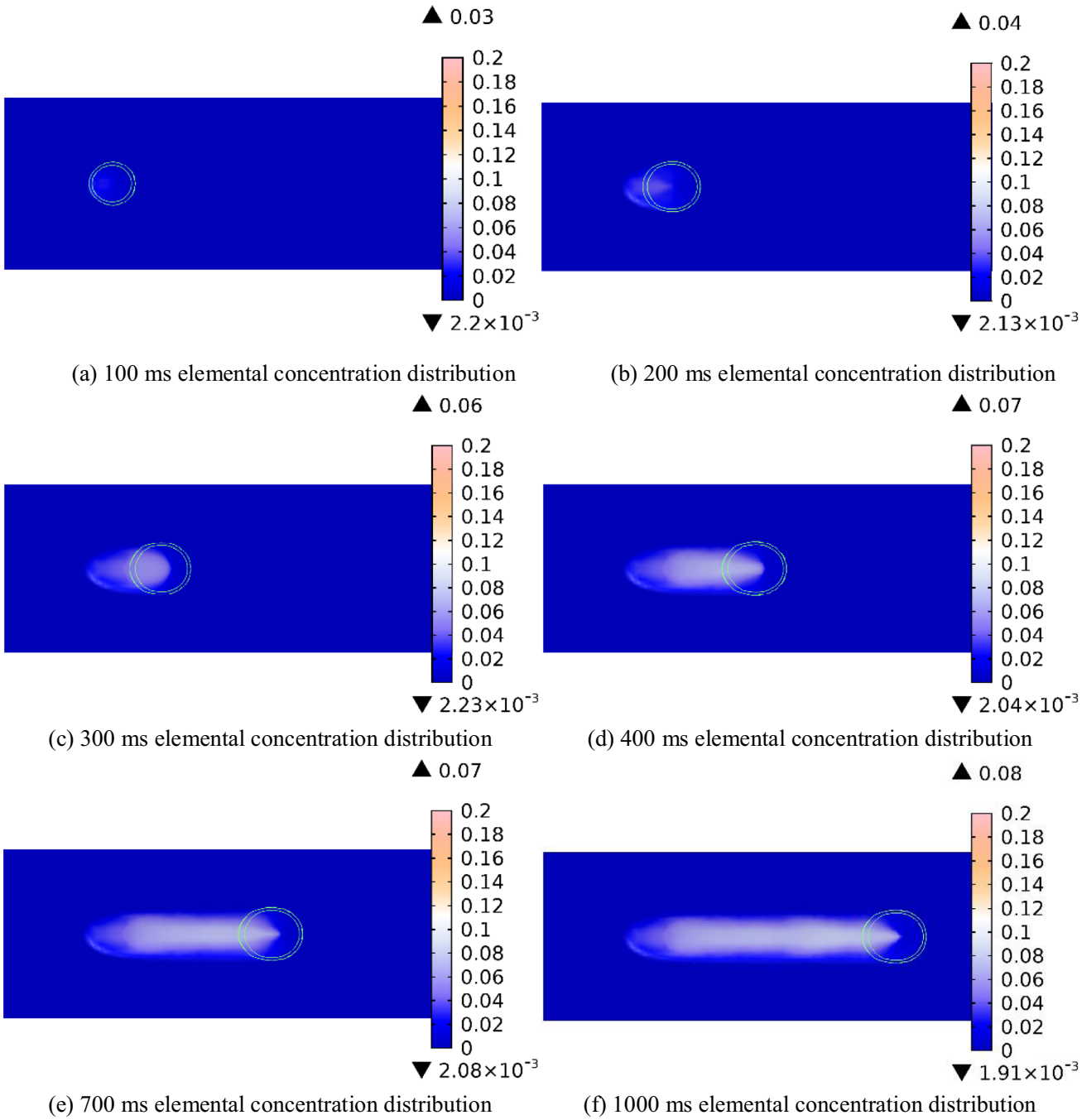

(a) 100 ms elemental concentration distribution

(b) 200 ms elemental concentration distribution

(c) 300 ms elemental concentration distribution

(d) 400 ms elemental concentration distribution

(e) 700 ms elemental concentration distribution

(f) 1000 ms elemental concentration distribution

Fig. 22 Cloud map of Cr concentration distribution at different moments

when the laser power is 1000 W is shown in Fig. 23. The figure shows that the Ni element content is 2% at 100 ms, at the initial stage of melting and cladding. At 200 ms, the molten pool is initially formed, and the elemental Ni content increases to 3%. At 300 ms, the molten pool is fully formed, and the elemental Ni content increases to 4%. At 500 ms, the molten pool gradually increased, and the maximum Ni element concentration reached 5%. And from 500 to 1000 ms, the Ni element concentration maxima varied less. Calculations show that the Ni element in the clad layer shows a gradual increase as the cladding work proceeds.

To obtain the distribution of each element at different locations in the molten layer, straight line 8, straight line 9, and straight line 10 are set, as shown in Fig. 24. The data are extracted for different elements distributed on different straight lines and plotted on a graph.

The variation curves of element Fe, element C, element Ni, and element Cr on straight line 8 are shown in Fig. 25.

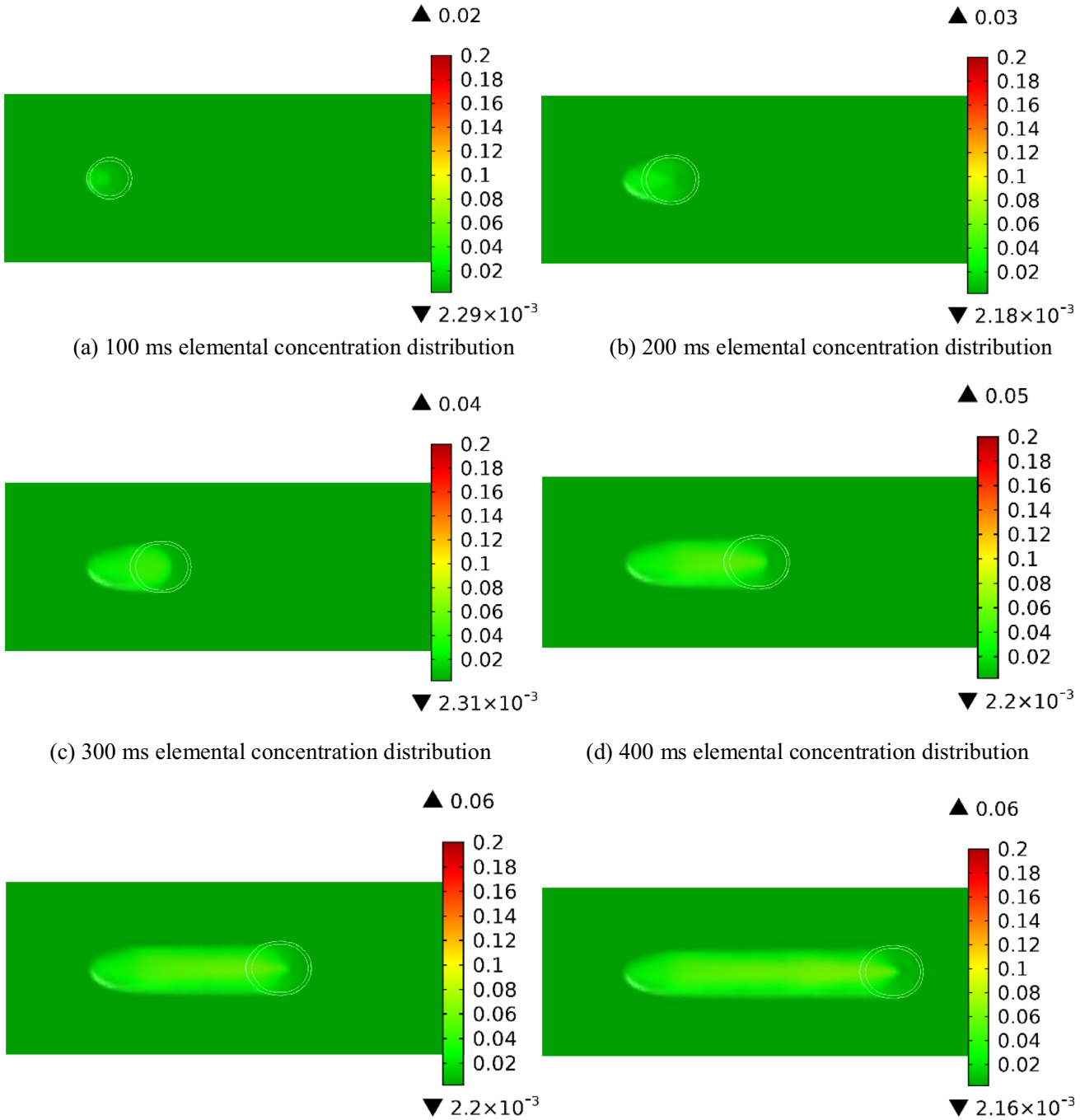

(a) 100 ms elemental concentration distribution

(b) 200 ms elemental concentration distribution

(c) 300 ms elemental concentration distribution

(d) 400 ms elemental concentration distribution

(e) 700 ms elemental concentration distribution

(f) 1000 ms elemental concentration distribution

Fig.23 Cloud map of Ni concentration distribution at different moments

The figure shows that the initial stage of cladding is in the range of 2–4 mm, and the concentration of each element in the clad layer changes slowly. This is because at the early stage of cladding, the molten pool is not fully formed, the molten pool flow rate is small, and the liquid metal in the molten pool is not very fluid. At the 4-mm position, the molten pool is fully formed, and the concentration of each element shows a small fluctuation with position. At the end of the cladding layer, the content of each element changes sharply. After the molten pool reaches the steady state, the

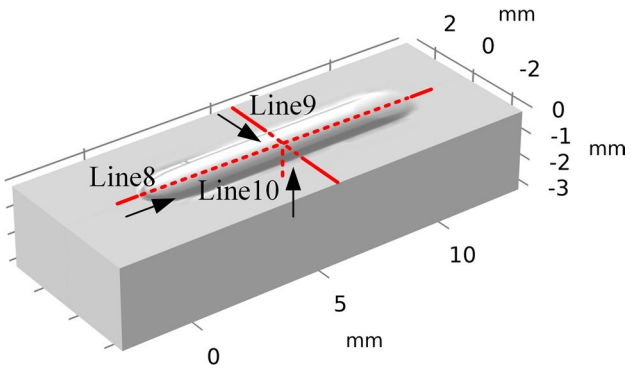

Fig. 24 Extraction location of element diffusion data

content of Fe and C elements increases, and the content of Ni and Cr elements decreases as the laser power increases. This is because the higher the laser power, the larger the irradiated area, the more the base material to be melted, and the smaller the range of variation of each element in the case of the same amount of powder feeding.

The distribution of the concentration of each element on straight line 9 is shown in Fig. 26. The figure shows that the greatest range of variation in the content of each element is found in the central region of line 9. The variation in the concentration of each element diminishes as the position approaches the sides of the cladding layer. As the laser

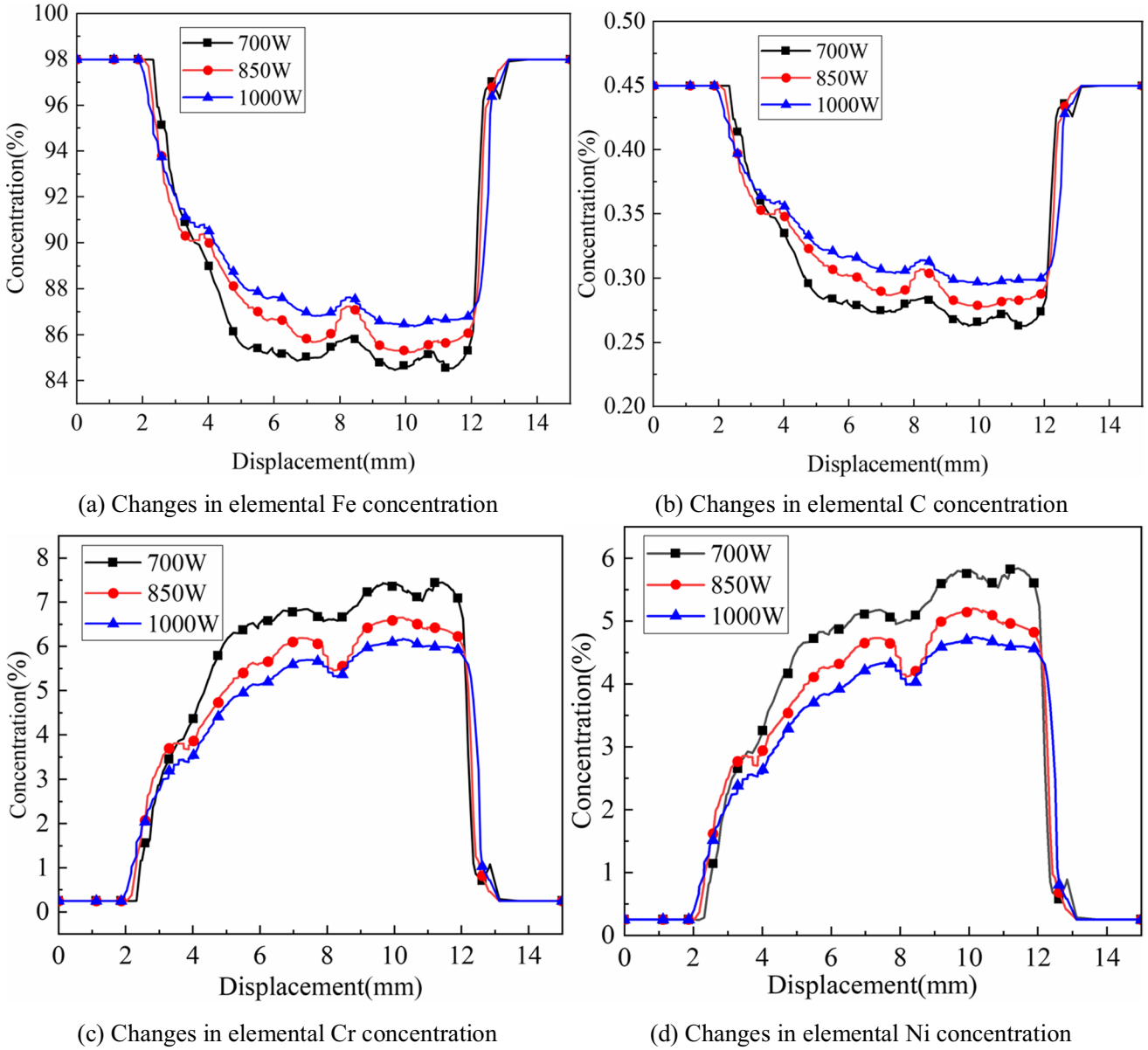

(a) Changes in elemental Fe concentration

(b) Changes in elemental C concentration

(c) Changes in elemental Cr concentration

(d) Changes in elemental Ni concentration

Fig. 25 Distribution curve of different elements on line 8

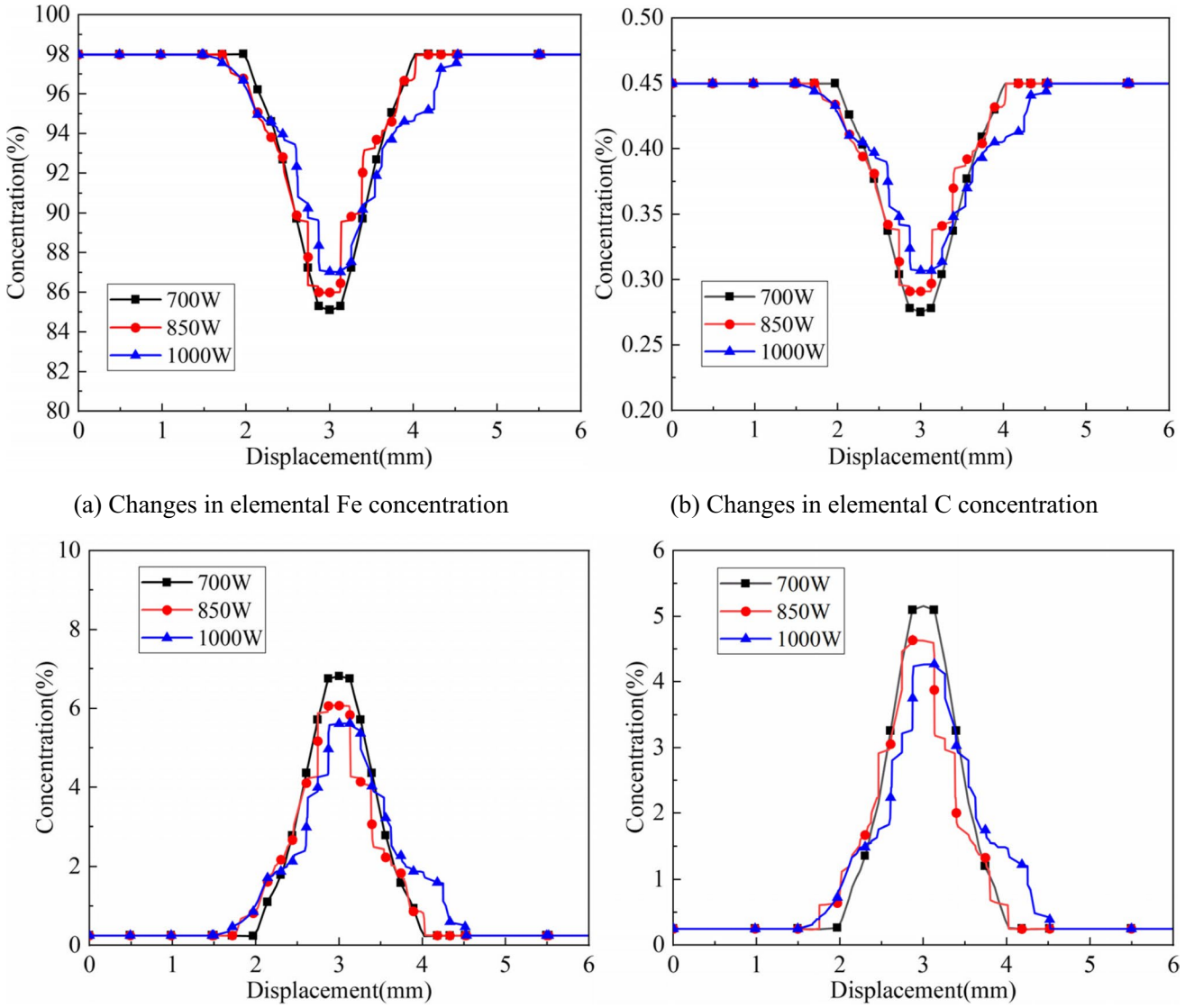

(a) Changes in elemental Fe concentration

(b) Changes in elemental C concentration

(c) Changes in elemental Cr concentration

(d) Changes in elemental Ni concentration

Fig. 26 Distribution curve of different elements on line 9

power increases, the range of variation of the concentration of each element in the molten layer decreases.

The distribution of the different element concentrations on straight line 10 is shown in Fig. 27. It can be seen in the figure that the range of variation of each element on the straight line 10 decreases as the laser power increases. The element concentration variation tends to stabilize when the position is close to the surface of the cladding layer.

The principle of metal solidification plays a pivotal role in the cladding process, particularly during techniques like laser cladding. As the laser beam irradiates the substrate, creating a localized, high-energy density zone, the material undergoes melting to form a molten pool. Subsequent to this, the metal solidification principle governs the intricate process of solidifying the molten pool. This involves the formation of specific microstructural features, such as dendritic growth and solidification structure, often characterized by an austenitic dendritic structure. The control of solidification rates is paramount, influencing the size and distribution of crystalline structures, which, in turn, dictate the mechanical and wear-resistant properties of the cladding layer. Moreover, the solidification process is intricately tied to the constraint effects, further shaping the

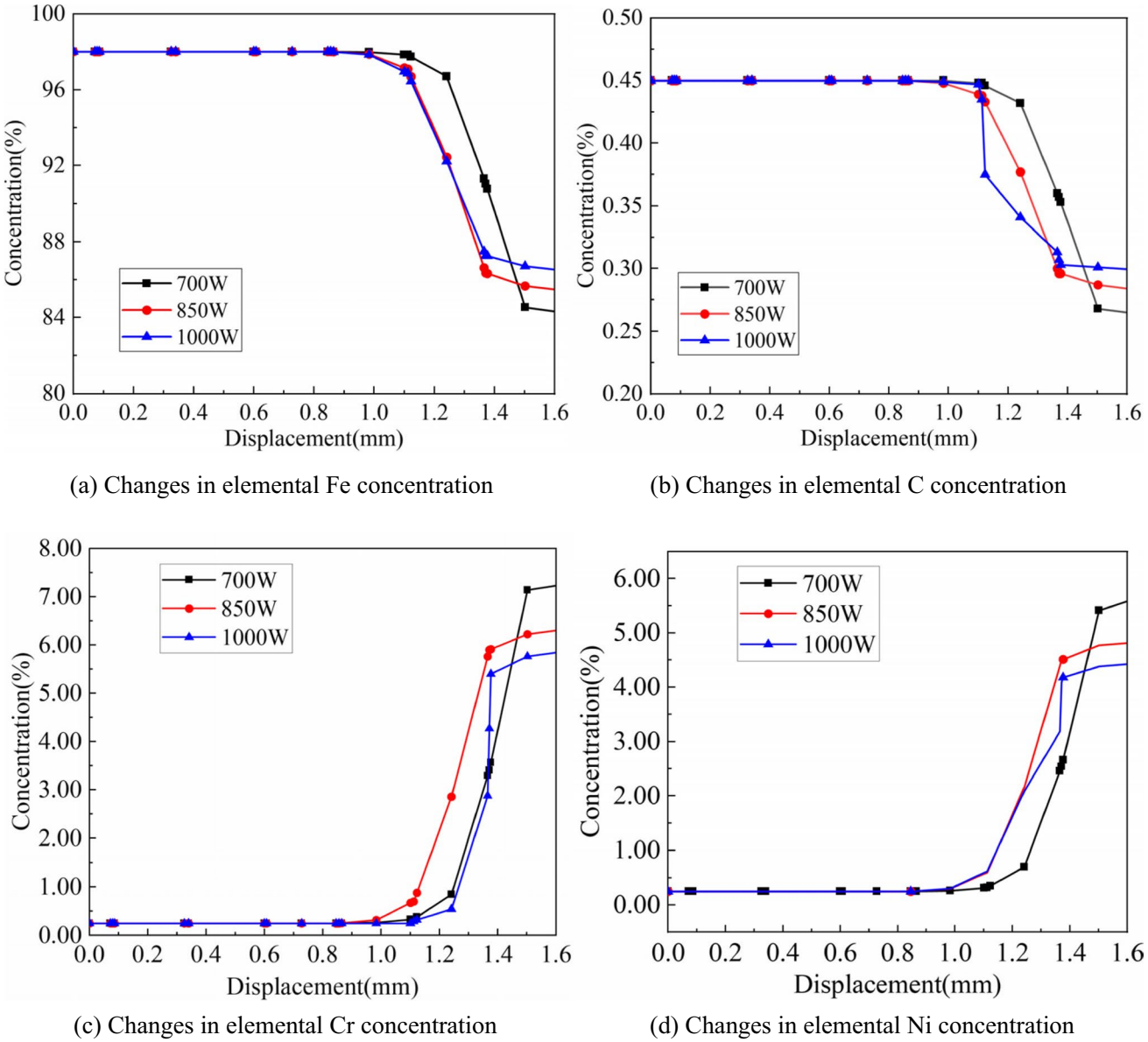

(a) Changes in elemental Fe concentration

(b) Changes in elemental C concentration

(c) Changes in elemental Cr concentration

(d) Changes in elemental Ni concentration

Fig. 27 Distribution curve of different elements on line 10

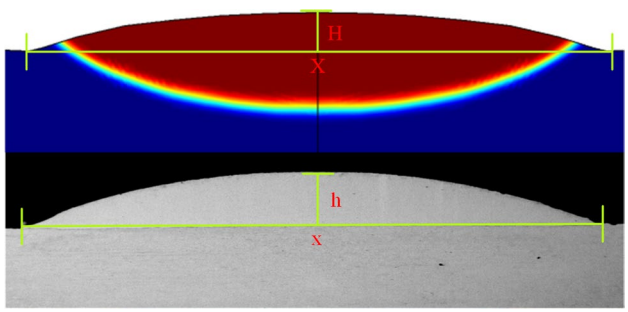

Fig. 28 Comparison between simulation and experiment

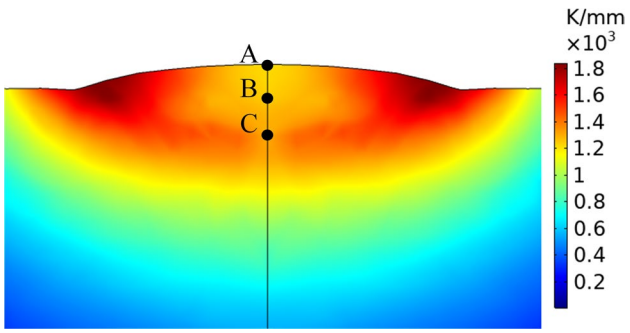

Fig. 29 Temperature gradient of molten pool

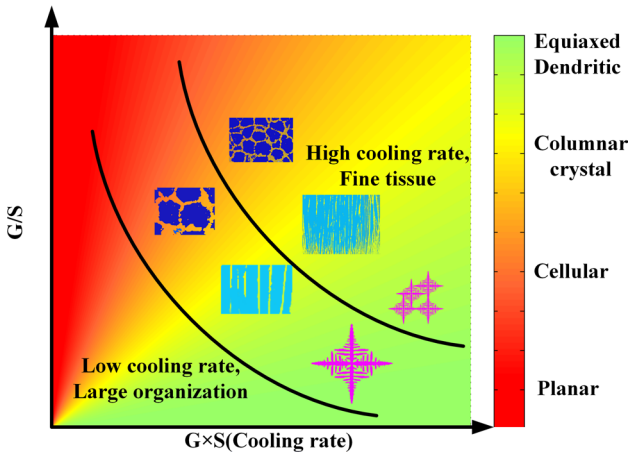

Fig. 30 Effects of G×S and G/S on microstructure

Table 4 G×S and G/S at different positions

Point	Numerical value	
	G×S(K/s)	G/S(K·s/mm^2)
A	11,897	124
B	6142	247
C	1295	1292

microstructure and performance of the clad layer. A profound understanding of the metal solidification principle is essential for optimizing laser cladding processes, ensuring enhanced material properties and performance.

4 Experimental research and validation

Scanning electron microscopy was used to observe the cross-sectional appearance profile of the molten cladding. The experimental observations are compared with the numerical calculations, as shown in Fig. 28. The upper part is divided into numerical model calculation results, the cladding layer height is $H=0.3031$ mm, the cladding layer width is $X=2.7534$ mm. The lower part is divided into the appearance profile of the cladding layer observed by scanning electron microscopy. The height of the cladding layer is $h=0.3294$ mm, and the width of the cladding layer is $x=2.7743$ mm. The comparison results show that the height error of the cladding layer is 8.01% and the width error is 0.75%, which is within a reasonable range. The height of the cladding layer contour fits, which verifies the validity of the numerical model.

The two key factors affecting the solidification organization are the current temperature gradient G and the solid–liquid interface migration rate S [24], which is expressed as

$$\begin{cases} G = \frac{\Delta T_d}{\Delta d} \\ S = V cos\theta \end{cases} \tag{18}$$

where Δd is the unit length, ΔT_d is the temperature change of Δd, and θ is the solidification growth rate and the laser scanning direction angle. According to the principle of metal solidification, it is known that the closer to the top of the molten pool, the smaller the θ and the larger the S. The solidification growth rate of the molten metal increases gradually from the bottom of the molten pool toward the surface of the molten pool in the region where S and V intersect with the substrate approximately vertically [25, 26]. The temperature gradient G is obtained by numerical calculation, as shown in Fig. 29. The cooling rate (G×S) affects the microstructure size, and high cooling rate can refine the grain. The shape control factor (G/S) determines the microscopic morphology, as shown in Fig. 30. The values of G×S and G/S at different locations in the molten layer are shown in Table 4.

The microscopic morphology of the molten layer is shown in Fig. 31. The point A is located at the top of the cladding layer, which has a larger G×S value and a smaller G/S value. The microstructure is mainly equiaxed crystals. The point B is located in the middle of the cladding layer, and the G×S value and G/S value are in the middle value. The microstructure is mainly composed of columnar crystals and equiaxed crystals. The point C is located at the bottom of the cladding layer, which has a smaller G×S value and a larger G/S value. In the microstructure, plane and cellular crystals coexist. The comparison analysis shows that the experimental observation results are basically consistent with the numerical calculation results, which further verifies the validity of the numerical model.

5 Conclusion

The calculated results analysis of the numerical model for laser cladding led to the following conclusions:

(1) The molten pool size is related to the laser power during the cladding. The higher the laser power, the higher the melting temperature and the larger the molten pool size. On the front side of the molten pool, the temperature gradient is larger. On the back side of the molten pool, the temperature gradient is smaller.
(2) The flow rate of molten pool is related to the laser power. The higher the laser power, the more pronounced the Marangoni effect and the smaller the flow rate in the center of the molten pool. As the laser power increases, the molten pool size becomes larger and the flow rate distribution of molten pool becomes larger.

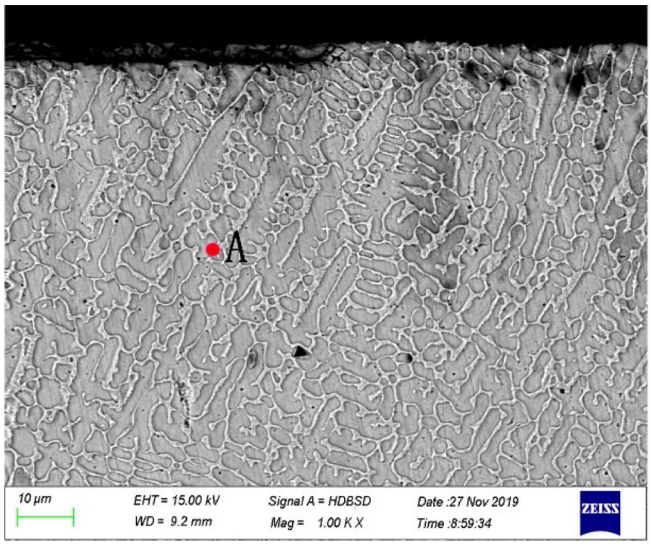

(a) Microstructure of point A location

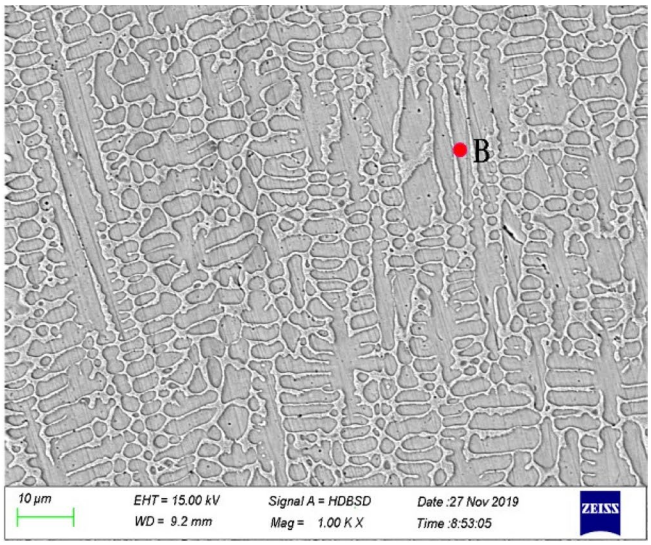

(b) Microstructure of point B location

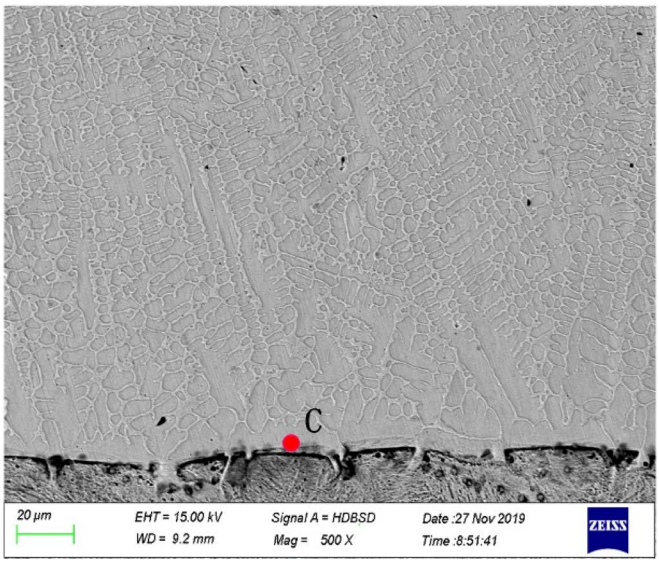

(c) Microstructure of point C location

Fig. 31 Microscopic morphology of cladding layer

(3) Due to the difference in the thermal physical parameters of the substrate and powder material, there is thermal deformation in the cladding process, which leads to large stresses on both sides of the cladding layer during the solidification for the molten pool. As the laser power increases, the heat-affected zone of cladding increases, and the distribution range for plastic stress increases.

(4) The concentration distribution of each element in the cladding layer varies with time, and the distribution of each element tends to be stable at 500 ms. The center and back of the molten pool with a high degree for element mixing. Influenced by the flow of molten metal, where the cladding layer is bonded to the substrate, the element content changes less. The surface area of the cladding layer with a large variation in element content.

Funding This work was supported by Applied Basic Research Project of Liaoning Province (2023JH2/101300226).

Declarations All analyses were based on previously published studies; thus, no ethical approval and patient consent are required. All authors

agree with the participation and publication of this article. We declare that we do not have any commercial or associative interest that represents a conflict of interest in connection with the work submitted.

References

1. Wang Q, Shi J, Zhang L et al (2020) Impacts of laser cladding residual stress and material properties of functionally graded layers on titanium alloy sheet[J]. Addit Manuf 35:101303
2. Xie H, Yang K, Li F et al (2020) Investigation on the Laves phase formation during laser cladding of IN718 alloy by CA-FE[J]. J Manuf Process 52:132–144
3. Zhao J, Wang G, Wang X et al (2020) Multicomponent multiphase modeling of dissimilar laser cladding process with high-speed steel on medium carbon steel[J]. Int J Heat Mass Transf 148:118990
4. Huang YL, Yang YQ, Wei GQ et al (2008) Boundary coupled dual-equation numerical simulation on mass transfer in the process of laser cladding[J]. Chin Opt Lett 6(5):356–360
5. Fallah V, Alimardani M, Corbin SF et al (2011) Temporal development of melt-pool morphology and clad geometry in laser powder deposition[J]. Comput Mater Sci 50(7):2124–2134
6. Hu YW, He XL, Yu G et al (2012) Heat and mass transfer in laser dissimilar welding of stainless steel and nickel[J]. Appl Surf Sci 258(15):5914–5922
7. Gan Z, Gang Y, He X et al (2017) Numerical simulation of thermal behavior and multicomponent mass transfer in direct laser deposition of co-base alloy on steel[J]. Int J Heat Mass Transf 104:28–38
8. Wirth F, Wegener K (2018) A physical modeling and predictive simulation of the laser cladding process[J]. Addit Manuf 22:307–319
9. Li C, Yu ZB, Gao JX et al (2019) Numerical simulation and experimental study on the evolution of multi-field coupling in laser cladding process by disk lasers[J]. Welding in the world 63(4):925–945
10. Song B, Yu T, Jiang X et al (2019) Numerical model of transient convection pattern and forming mechanism of molten pool in laser cladding[J]. Numer Heat Transf Appl 75(12):855–873
11. Liu H, Li M, Qin X et al (2019) Numerical simulation and experimental analysis of wide-beam laser cladding[J]. Int J Adv Manuf Technol 100(9–12):1–13
12. Asai S, Muchi I (1978) Theoretical analysis and model experiments on the formation mechanism of channel-type segregation[J]. Tetsu-to-Hagane 18(2):90–98
13. Bennon WD, Incropera FP (1987) A continuum model for momentum, heat and species transport in binary solid-liquid phase change systems-I. Model formulation[J]. I J Heat Mass Transf 30(10):2161–2170
14 Bennon WD, Incropera FP (1987) A continuum model for momentum, heat and species transport in binary solid-liquid phase change systems-II. Application to solidification in a rectangular cavity[J]. Int J Heat Mass Trans 30(10):2171–2187
15. Deus AM, Vilar R (1996) One-dimensional thermal model including the dependence of absorptivity on temperature using Hagen-Rubens equation[J]. Laser Proc Surf Treat Film Deposit 307:195–201
16. He X, Song L, Yu G et al (2011) Solute transport and composition profile during direct metal deposition with coaxial powder injection[J]. Appl Surf Sci 258(2):898–907
17. Morville S, Carin M, Peyre P et al (2012) Longitudinal modeling of heat transfer and fluid flow during multilayered direct laser metal deposition process[J]. J Laser Appl 24(3):032008–032017
18. Li C, Yu ZB, Gao JX et al (2019) Numerical simulation and experimental study on the evolution of multi-field coupling in laser cladding process by disk lasers[J]. Weld World 63(4):925–945
19. Bedenko D, Kovalev O, Smurov I et al (2016) Numerical simulation of transport phenomena, formation the bead and thermal behavior in application to industrial DMD technology[J]. Int J Heat Mass Trans 95:902–912
20. Fang L, Yao JH, Hu XX et al (2011) Effect of laser power on the cladding temperature field and the heat affected zone[J]. J Iron Steel Res, Int 18(1):73–78
21. Hao M, Sun Y (2013) A FEM model for simulating temperature field in coaxial laser cladding of TI6AL4V alloy using an inverse modeling approach[J]. Int J Heat Mass Trans 64:352–360
22. Jendrzejewski R, Śliwiński G, Krawczuk M et al (2006) Temperature and stress during laser cladding of double-layer coatings[J]. Surf Coatings Technol 201(6):3328–3334
23. Curtiss CF, Bird RB (1999) Multicomponent diffusion[J]. Ind Eng Chem Res 38(7):2515–2522
24. Long R (2007) Effects of scanning methods on thermal stress during laser metal deposition shaping[J]. Chin J Mech Eng 43(11):74–81
25. Reddy L, Preston SP, Shipway PH et al (2018) Process parameter optimisation of laser clad iron based alloy: predictive models of deposition efficiency, porosity and dilution[J]. Surf Coatings Technol 349:198–207
26. XiaoMing C, HaiJin W, XiaLiang Z et al (2018) Laser surface modification technology and research progress[J]. Mater Rev 32(S1):341–344